

# A Comprehensive Characterization of the Vacuum Beam Guide and Its Applications

Yuexun Huang,<sup>1,\*</sup> Delaney Smith,<sup>1</sup> Pei Zeng,<sup>1</sup> Debayan Bandyopadhyay,<sup>1</sup> Junyu Liu,<sup>2</sup> Rana X Adhikari,<sup>3,†</sup> and Liang Jiang<sup>1,‡</sup>

<sup>1</sup>*Pritzker School of Molecular Engineering, The University of Chicago, Chicago, IL 60637, USA*

<sup>2</sup>*Department of Computer Science, The University of Pittsburgh, Pittsburgh, PA 15260, USA*

<sup>3</sup>*Division of Physics, Math, and Astronomy, LIGO Laboratory, California Institute of Technology, Pasadena, CA 91125 USA*

(Dated: November 26, 2025)

The proposed vacuum beam guide (VBG) represents an innovation in the field of quantum channel technology, guaranteeing an ultra-low level of attenuation and a broad transmission linewidth, which offers an unprecedented quantum capacity exceeding Tera-qubits per second on a continental scale. However, its stability in terms of interferometry remains unexamined. To address this gap, we have developed a comprehensive error model that captures the intrinsic phase noise power spectral density associated with VBG, thereby revealing the advantages of VBG for interferometry over existing techniques. This model facilitates a comprehensive characterization of VBG as a photonic quantum channel, thereby facilitating a detailed investigation of its potential. Our theoretical analysis demonstrates the feasibility of VBG and its expected performance in a wide range of quantum applications.

## I. INTRODUCTION

Creating a low-loss quantum channel for global networks is challenging due to optical absorption losses that restrict fiber and free-space channels to tens of kilometers [1–4]. This causes an exponential drop in direct quantum communication rates over long distances. While improvements in quantum communication range have been made, current satellite-based channels are costly, fragile, and weather-dependent [5–8]. Quantum repeaters lack full error correction ability, and their use results in a polynomial decline in communication rate across long distances[9].

An entirely distinct approach to counteracting the attenuation encountered in bosonic channels is provided by the vacuum beam guide (VBG) [10]. This approach holds substantial promise for establishing the fundamental framework of a global-scale quantum network due to its inherent resilience and practicality, all of which can be achieved using current technology. Bosonic channel specifications typically highlight key metrics, including attenuation, transmission linewidth, interference stability, polarization, transmission delay, and dispersion. The first three are crucial for defining the noise model of the quantum channel and thus the quantum capacity across various coding schemes [11–15], while other metrics may serve specific needs. By conceptualizing the VBG as a pure loss channel [11, 14], the quantum channel capacity is projected to exceed terabits per second in terms of qubits, which is asymptotically attainable with the appropriate implementation of phase-insensitive dual-rail encoding [16]. Nevertheless, certain scenarios pose chal-

lenges in performing or modifying such encodings, particularly within the domain of quantum metrology, where information is intrinsically encoded by nature. In these cases, achieving interference stability is crucial to overcome the dephasing that would destroy any prospective quantum attributes[17, 18].

A comprehensive description of VBG as a bosonic channel is essential, as it forms the groundwork for investigating potential applications and allows for the relaxation of constraints on encoding schemes. The stability of the VBG as a set of interferometers can be evaluated using the phase noise power spectral density (PSD), denoted  $S_\phi(f)$  [19, 20]. This PSD is composed of dozens of noise sources, including both fundamental and technical aspects. Typically, the PSD associated with a particular noise source is derived from small-scale characterization experiments and/or detailed models. The noise sources are separated in this way for the ease of analysis. It is assumed in most cases that the noise from each source is random and statistically uncorrelated with any others. Leveraging early theoretical insights from LIGO and practical performance data from the O1-O4 observational runs [21–23], we have managed to develop a comprehensive phase noise model for VBG. Although unsurprising, given LIGO’s stringent stability demands for gravitational wave detection [24], the estimated performance illustrates notable advantages beyond 10 Hz over the limit set by the fiber thermal noise floor, even while using considerably less complexity than LIGO.

This noise analysis enables us to identify direct applications that span the categories of secure quantum communication, distributed quantum sensing, and federated quantum computing. Our numerical investigations reveal a significant scaling enhancement, which clearly illustrates the versatile nature and substantial advantages conferred by VBG.

---

\* yesunhuang@uchicago.edu

† rana@caltech.edu

‡ liangjiang@uchicago.edu

## II. CHARACTERIZATION OF VBG

The VBG utilizes an array of precisely aligned lenses and mirrors within an extremely long vacuum tube to guide the quantum signals encoded in photons, a sketch of which is shown in Fig. 1(a). VBG is composed of  $N_{\text{tot}}$  sections, each with a length of  $L_0$ , and lenses with a radius of  $R$  placed at both ends to guide the light signal over a distance of  $L_{\text{tot}} = N_{\text{tot}}L_0$ . In order to traverse a continent, the light will need to bend to avoid existing structures and save on construction costs. Flat steering mirrors will be mounted inside the tube to enable these static deflections as well as provide active steering. The entire system can be operated at room temperature while maintaining a nominal vacuum pressure of no more than 1 Pa to ensure low absorption and perturbation of the residual gas in the tube. This baseline design is summarized in Table. I [10]. Such a configuration serves as the foundation for estimating the performance metrics, the values of which, together with the relevant applications, are summarized in Fig. 3.

TABLE I. Nominal Parameters of VBG

Parameters	Symbol	Values
Section Length	$L_0$	4 km
Focus Length	$f$	2 km
Lens Radius	$R$	12 cm
Center Wavelength	$\lambda_c$	1550 nm
Spot Size	$w$	4 cm
Operating Pressure	$P$	1 Pa
Operating Temperature	$T$	$\sim 300$ K

### A. Attenuation

As the beam travels through mostly vacuum in the VBG, it is an ultra-transparent channel with extremely low loss at the level of  $\sim 10^{-5}$  dB/km. In addition, compared to satellite-to-ground links, VBG is ground-based, stable, robust against environmental disturbances, and can be operated at all times. Most importantly, VBG does not suffer from the baseline 3 dB loss introduced by the thickness of the atmosphere, which is almost inevitable for satellite-to-ground links [5]. The total effective attenuation of VBG,  $\alpha_{\text{tot}}(\lambda)$ , in the normalized unit of dB/km, can be divided into the following four main contributions,

$$\alpha_{\text{tot}}(\lambda) = \alpha_{\text{lens}} + \alpha_{\text{gas}} + \alpha_{\text{align}} + \frac{L_0}{L_{\text{mirr}}} \alpha_{\text{mirror}}, \quad (1)$$

where  $\alpha_{\text{lens}}$  denotes the total loss of the lens due to absorption, scattering, diffraction, and reflection;  $\alpha_{\text{gas}}$  is the loss of the residue gas, dominated by absorption;  $\alpha_{\text{align}}$  is due to the imperfect alignment of the lens, which leads to the leakage of energy into higher-order transverse modes. This loss mechanism mentioned above constitutes the baseline loss of VBG channels, as estimated

in the previous literature [10]. However, in reality, one may need reflector devices over a certain length  $L_{\text{mirror}}$  to deflect the beam and overcome Earth's curvature or to accommodate environmental conditions. The angular alignment of such a device is crucial and may impose additional loss, which is captured in the last term. We provide two different reflector designs, namely single-45°-mirror (S45M) and two-mirror rigid-retroreflector (TM-RRR), each of which is analyzed in detail in Appendix. A.

The attenuation spectrum of the VBG around the telecom band, assuming the default configuration, is numerically calculated and plotted in Fig. 1(b), compared to the state-of-the-art fiber and satellite-to-ground channel, which shows a low-loss telecom passband centered at  $\lambda_c \approx 1550$ nm with at least two orders of magnitude improvement. The average attenuation rates concerning the wave number under different models within the pass window are calculated for later usage, respectively, as follows,

$$\bar{\alpha}_{\text{VBG}} \approx 3.7 \times 10^{-5} \text{ dB/km}; \quad (2)$$

$$\bar{\alpha}_{\text{VBG(S45M)}} \approx 1.0 \times 10^{-4} \text{ dB/km},$$

$$\Delta \bar{\alpha}_{\text{VBG(S45M)}} \approx 6.3 \times 10^{-5} \text{ dB/km}; \quad (3)$$

$$\bar{\alpha}_{\text{VBG(TMRRR)}} \approx 4.0 \times 10^{-5} \text{ dB/km},$$

$$\Delta \bar{\alpha}_{\text{VBG(TMRRR)}} \approx 3.0 \times 10^{-6} \text{ dB/km}. \quad (4)$$

### B. Linewidth

In addition to the ultra-low attenuation achieved at the center frequency, the linewidth, or transmission window, is crucial for time, frequency, or hybrid division multiplexing and thus directly contributes to the total quantum capacity. The VBG attenuation spectrum suggests a broad linewidth of roughly  $\Delta\lambda = 50$ nm or  $\Delta\nu \approx \frac{c\Delta\lambda}{\lambda_c^2} = 6$ THz, across which VBG maintains its average attenuation factor calculated in the previous section. The transmission efficiency at a given wavelength  $\lambda$  can be determined using the attenuation factor as  $\eta(\lambda) = 10^{-0.1L_{\text{tot}}\alpha(\lambda)}$ . Following this, the pure-loss capacity per channel use is defined as [11, 12, 14, 25]:

$$q_k(\lambda) = \max \left[ \log_2 \left( \frac{\eta^{2-k}(\lambda)}{1 - \eta(\lambda)} \right), 0 \right], \quad (5)$$

where  $k = 1, 2$  corresponds to one- or two-way quantum communication. Notably, the one-way model is shown to be constructively realizable with appropriate encoding [26].

Therefore, the maximum transmission rate of quantum information through multiplexing in quantum communication protocols can be obtained in units of qubits per second by integrating  $q_k$  into the attenuation spectrum[13]:

$$Q_k \equiv \int q_k d\nu = \int q_k(\lambda) \frac{c}{\lambda^2} d\lambda. \quad (6)$$

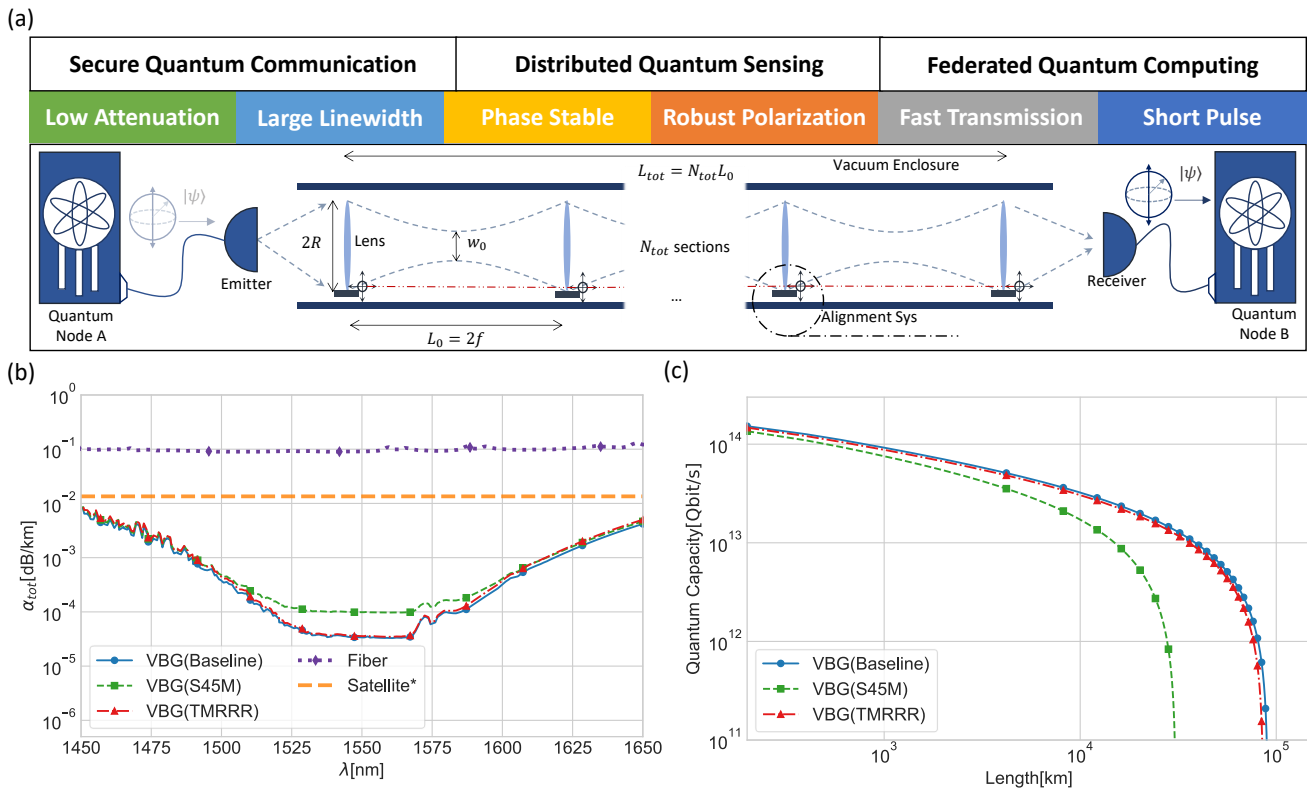


FIG. 1. The illustration and performance of VBG and additional loss from different reflector models (S45M and TMRRR) under room temperature and a residue gas pressure of  $P = 1\text{Pa}$ . The alignment relative accuracy of each lens and mirror is assumed to be 0.1% for translation and 1%. (a) The basic design of VBG promises outstanding performance across various metrics supporting a wide range of quantum applications. (b) The attenuation factor of VBG compared to the SOTA fiber (Experimental data presented here while theoretical limit is greater than 0.01dB assuming practical constrains) [1, 2] and the satellite-to-ground link (\*approximate level) [5, 7]. (c) The quantum capacity of VBG under one-way protocols (Two-way protocols show similar results).

The wide transmission windows of VBG enable it to achieve a remarkable capacity at the Tera-qubit/second level over a continental distance ( $10^4\text{km}$ ) for both reflector designs, as demonstrated in Fig. 1 (c). Quantitative evaluation of VBG's channel capacity demonstrates substantial superiority compared to state-of-the-art satellite-based systems by at least four orders of magnitude [5, 10].

### C. Phase Noise Power Spectral Density

Phase noise is typically regarded as less significant than attenuation loss because straightforward coding strategies, such as time-bin encoding or prevalent polarization encoding, can mitigate it when a bosonic channel is used for quantum communication. Nonetheless, this poses a constraint when using VBG as the foundation for global-scale quantum networks: the secondary channels linked to VBG might implement distinct coding methods, such as GKP codes [16, 27–29], to counteract loss; yet they are less robust against phase noise, necessitating a coding conversion that unavoidably diminishes quantum fidelity. Numerous QKD protocols also use single rail encoding

to improve communication distance and security [30–33]. More critically, in quantum sensing schemes, the encoding is typically intrinsic to the sensing entity and is sensitive to both attenuation and phase noise [34, 35]. Converting between coding schemes can compromise quantum advantages or restrict parameter ranges. Therefore, the phase stability performance of the VBG channel is essential for its versatility.

Noise sources corresponding to a particular application scheme can be broadly classified into two main categories: channel-added noises and those associated with source-detection processes. The former refers to the intrinsic noise attributed to the VBG channel itself, while the latter stems from the quantum sources and the details of detection methodologies, including examples such as dark noise, fluctuations in the laser source's amplitude/frequency, and shot noise, which are not directly related to the channel characteristics. This section is dedicated to estimating only the channel-added noise, as the noise associated with quantum sources and detection methods is determined by the specific application scheme.

Unlike attenuation noise, the total phase noise for cer-

tain applications is not always the overall rms noise but is rather determined by the signal frequency band of interest, since the noise outside the band can always be filtered out by either a lock-in amplifier or post-data analysis. Thus, the phase noise power spectral density (PNPSD),  $S_\phi(f)$ , shall be characterized for general application. In addition, we normalize the amplitude spectral density (ASD, square root of the PSD) with the total distance to obtain  $\sqrt{\hat{S}_\phi}$  in the unit of  $(\text{rad}/\sqrt{\text{Hz} \bullet \text{km}})$ , assuming that the noises from each VBG section are random and uncorrelated under the section-wise stabilization scheme after subtracting the active detection by sections. The overall phase noise power spectral density of VBG under the default configuration is shown in Fig. 2 (a) compared to the dominant thermal noise of fibers, where the contributions can be further divided into alignment and seismic noise, residual gas noise, thermal noise, and so on; the details of these contributions are included in Appendix. B. It is observed that VBG demonstrates advantages over fiber when the frequency is above 10Hz: The ASD scales roughly as  $\frac{1}{f^3}$  from 1Hz to 1kHz due to the passive isolated seismic noise, after which the residue gas scattering causes a bump around 10kHz, followed by the flattening at high frequency introduced by mirror thermal noise. Fortunately, low-frequency noise below the cutoff frequency  $\sim c/2L_0 \approx 30\text{kHz}$  can be suppressed by the round-trip phase noise cancelation technique [36], as shown by the red-triangle line, which is, in turn, dominated by phase detection noise. The integration of  $S_\phi(f)$  over the specified signal band gives rise to the dephasing factor  $\gamma$  in the common quantum information literature [15]. For typical DC signals with a finite averaging window  $\tau$ , integration is effectively conducted from 0.01Hz to an upper cutoff at  $f_h \sim 1/\tau$ , with cumulative noise under various cutoff frequencies plotted in Fig. 2 (b) (See Appendix. B 1 for the explanation of the lower cutoff frequency). The rms phase noise per square-root kilometer that integrates throughout the VBG spectrum before and after active subtraction is at the level of 2rad and 19 $\mu$ rad, respectively, demonstrating the phase robustness of the VBG system.

The phase stability of VBG can certainly be improved, given that it is currently inferior to advanced LIGO by at least 3 orders of magnitude in terms of rms movement [37, 38]. One of the reasons is that no real-time active feedback [39, 40] is employed in our configuration due to budgetary concerns. This can be improved without technical challenges if necessary.

#### D. Polarization, Transmission Speed and Pulse Duration

In addition to the three critical metrics introduced above, we also briefly discuss the performance of VBG in polarization maintenance, transmission speed, and the pulse duration limit, which might be less relevant in the

general case but are important for specific usages.

**Polarization** maintenance is also important for a quantum channel, as it is widely adopted in both satellite and fiber techniques. In polarization based dual-rail encoding, the degradation of fidelity arises from both amplitude and phase, which are coupled together and cannot be simply represented by attenuation or dephasing, as detailed in Appendix. B 4. The noise is mainly attributed to the misalignment of the reference plane of each optical element, and the net effects of each section of the channel, in addition to the overall average attenuation, can be approximately described by the following two nontrivial Kraus operators,

$$\{K_\alpha\} = \sqrt{p} \left\{ \begin{pmatrix} 0 & 1 \\ -1 & 0 \end{pmatrix}, \begin{pmatrix} 0 & e^{i\bar{\phi}} \\ -e^{-i\bar{\phi}} & 0 \end{pmatrix} \right\}, \quad (7)$$

where  $\bar{\phi} \sim 10^{-2}\text{rad}$  [44] is the average birefringence phase difference, and  $p$  can be computed by integrating over the relevant frequency range of the misalignment angle  $\delta\theta$ 's noise power spectrum as  $p = 2 \int_{f_{\min}}^{f_{\max}} S_\theta(f) df$ . One can also normalize the probability with 1/4km to get the effective dissipation coefficient, similar to the treatment in the previous section. The noise can also be suppressed with proper frequency filtering analysis. For a rough estimate of the worst-case effect, one can replace the integral with the rms value of  $\delta\theta_{\text{rms}} \sim 10^{-3}\text{rad}$  [45] per section, which gives rise to a probability of 1ppm and suggests that the polarization noise by VBG is two orders of magnitude smaller than the attenuation under the default configuration. This demonstrates the robustness of VBG in transmitting polarization-encoded qubits.

**Transmission speed** of the non-monochromatic signal will be slowed down by the dispersion in the VBG channel and is calculated as the group velocity,

$$v_g = \frac{\partial\omega}{\partial k} = \frac{c}{n} \left( 1 + \frac{\lambda}{n} \frac{\partial n}{\partial \lambda} \right) \equiv \frac{c}{n_g}. \quad (8)$$

Since most parts of the VBG are in a vacuum, the deviation from the speed of light in the vacuum shall come from the weighted average of the group velocity determined by the optical elements and the vacuum velocity as  $\bar{v}_g = \frac{L_0}{\sum_i d_i/v_{g_i}}$ , where  $\{d_i\}$  denotes the sections with different group velocity indices  $n_g$ . For our VBG system, the deviation is dominated by the ultra-pure silica substrate, which has a thickness of roughly  $d_{\text{substrate}} \approx 2\text{cm}$  for the worst-case consideration[46] and a group velocity index of  $n_g \approx 1.46$  for the light centered at 1550nm. Therefore, the average group velocity in VBG is calculated as

$$\bar{v}_g \approx (1 - 7 \times 10^{-6})c, \quad (9)$$

which represents only a 10ppm deviation and thus can be safely neglected under most circumstances.

**Pulse duration** will also be limited by the dispersion effects due to the spreading of the wave packet deter-

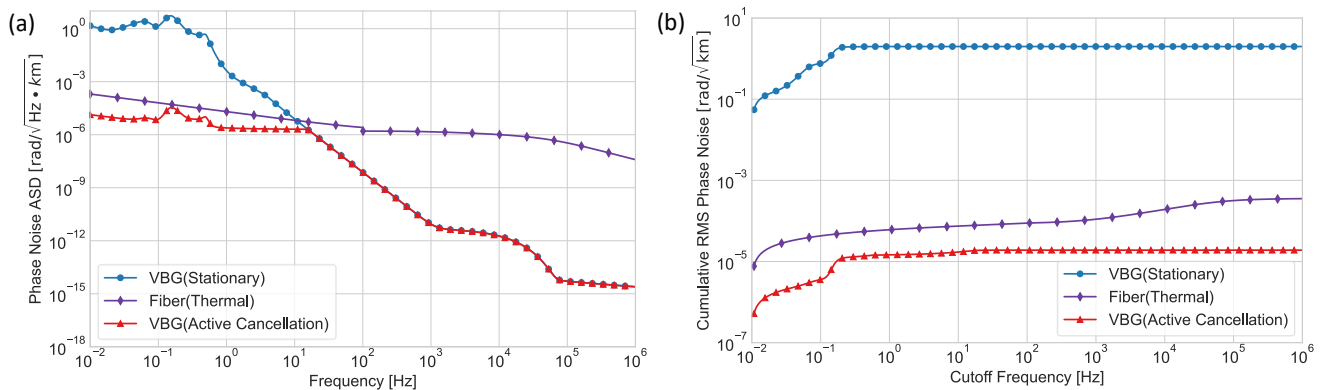


FIG. 2. Interference stability of VBG. The extra contributions from reflector is neglectable and thus are not shown here (See Appendix. B1). (a) Normalized phase noise power spectral density of the VBG before and after active cancellation in comparison with fiber thermal noise floor [41–43]. (b) Cumulative phase noise.

mined by the group-velocity dispersion (GVD) [47],

$$\text{GVD} \equiv \frac{\partial^2 k}{\partial \omega^2} = \frac{2}{c} \left( \frac{\partial n}{\partial \omega} \right) + \frac{\omega}{c} \left( \frac{\partial^2 n}{\partial \omega^2} \right). \quad (10)$$

As an unchirped beam with a Gaussian profile passing through relatively thick materials with a thickness of  $d_i$ , the expansion in pulse duration  $\tau$  can be calculated as

$$\Delta\tau \approx \frac{2\text{GVD}^2 d_i^2}{\tau^3}, \quad |\Delta\tau| \ll \tau. \quad (11)$$

The simulation shows that the group-velocity delay ( $\text{GDD} \equiv \text{GVD} \times d_i$ ) of the coating is at least two orders of magnitude smaller than that of the substrate. Therefore, the expansion effects are dominated by the silica substrate with  $\text{GVD} \approx -25.855 \text{fs}^2/\text{mm}$  at  $1550 \text{nm}$  [48]. Suppose that the beam goes through  $N \sim 10^4$  sections corresponding to a distance of  $10^4 \text{km}$ , and we require that the expansion of the duration is no larger than the original duration  $\tau_{\text{GVD}}$ . Then, the duration of the pulse is lower bounded by

$$N\Delta\tau < \tau_{\text{GVD}} \Rightarrow \tau_{\text{GVD}} \gtrsim 50 \text{fs}. \quad (12)$$

For comparison, the shortest pulse duration limited by the attenuation spectrum is given by

$$\tau_{\text{spectrum}} \geq \frac{1}{2\pi\Delta\nu} \sim 40 \text{fs}, \quad (13)$$

which is close to the value limited by the dispersion.

### III. NOTABLE APPLICATIONS

VBG’s capacity for ultra-low-loss bosonic quantum state transmission enables it to surpass the theoretical QKD key rate limit of the current satellite-to-ground systems by four orders of magnitude, and experimental results by eight orders under the basic QKD scheme [5, 10],

suggesting its unique benefits for secure quantum communication. Moreover, VBG’s high interference stability is crucial for overcoming significant hurdles in distributed quantum sensing, where naturally encoded signals typically experience phase noise that negates any quantum benefits [17, 18]. Regarding federated quantum computing, particularly in cloud computing contexts [84–86], VBG offers a key benefit of reducing transmission delays in addition to ensuring robust, high-bandwidth entanglement. With the summarized Fig. 3 of various protocols spanning the three key categories mentioned above, we highlight a detailed quantitative analysis for implementing Device-Independent QKD (DI-QKD) [49, 54, 56], Quantum Telescope (Q-Telescope) [68–70], and Blind Quantum Computation (BQC) [79, 80] with the VBG channel in this section to substantiate the claimed benefits. The detailed illustration and performance estimation for the other mentioned protocols can also be found in the corresponding sections in Appendix, as shown in the caption of Fig. 3 for interested readers.

#### A. Device Independent QKD

DI-QKD is a direct application of VBG. The key idea is that maximal two-body entanglement cannot be shared by a third party, which can be quantified by the CHSH score [49]. Although this avoids imposing any assumptions on the measurement and transmission devices for security, a non-zero secure key rate can only be obtained when the entanglement of the transmitted state is sufficient, thus setting a threshold for transmission efficiency. Unfortunately, the theoretical lower bound for CHSH-based protocols [87] is far above the coupling limit imposed by the 3dB atmosphere absorption using satellite-to-ground links [5].

We select the standard and simplest protocol for demonstration, which does not require any optimization of the experimental configuration but has a transmission

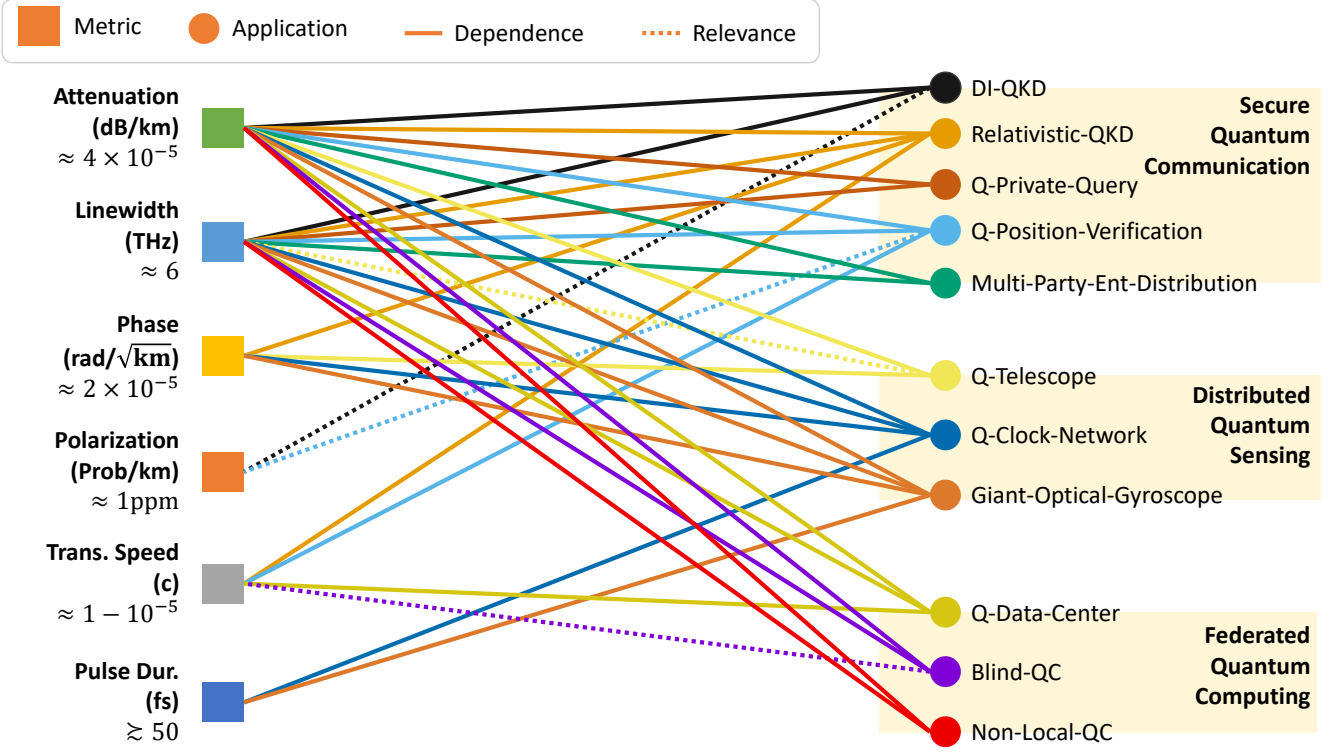


FIG. 3. Summary of VBG’s performance metrics and application requirements. The solid line indicates that the specific application depends on a certain performance metric, while the dotted line suggests that it may be relevant according to the concrete protocol. Here, the applications in the category of secure quantum computation include Device-Independent Quantum Key Distribution [49–57] (Sec. III A), Relativistic-QKD [31, 58] (Appendix. E 2), Quantum Private Query [59] (Appendix. E 2), Quantum Position Verification [60–62] (Appendix. E 1), and Multi-party Entangled State Distribution [63–67] (Appendix. E 2); Distributed quantum sensing covers Quantum Telescope [68–70] (Q-Telescope, Sec. III B), Quantum Clocks Network [71–73] (Appendix. E 3), and Giant Optical Gyroscope [74–76] (Appendix. E 4); And federated quantum computing consists of Quantum Data Centers [77, 78] (Appendix. E 5), Blind Quantum Computation [79, 80] (Sec. III C), and Non-Local Quantum Computation [81–83] (Appendix. E 6).

efficiency threshold of  $\eta_{\text{th}} \approx 90.8\%$  [54]. Analysis of other protocols can be conducted in a similar manner. The recipe for this DI-QKD protocol consists of the following steps,

1. **State Distribution.** The source prepares a state with two photons of the following form in the  $\sigma_z$  basis:

$$\rho_s = V \frac{1}{2} (|-, +\rangle - \langle -, +|)(\langle -, +| - \langle +, -|) + (1 - V) \frac{I}{2},$$

where  $V = \frac{4F-1}{3}$  denotes visibility, with  $F$  representing the fidelity of the state, which is then distributed to each party with an equal transmission efficiency of  $\eta = 10^{-0.1\bar{\alpha}L/2}$ .

2. **Measurement.** Alice randomly chooses an input  $x \in \{0, 1, 2\}$  and measures the state with the measurement operator  $\hat{A}_x \in \{\sigma_z, (\sigma_z + \sigma_x)/\sqrt{2}, (\sigma_z -$

$\sigma_x)/\sqrt{2}\}$ . Similarly, Bob randomly chooses an input  $y \in \{1, 2\}$  and measures the state with the measurement operator  $\hat{B}_y \in \{\sigma_z, \sigma_x\}$ . No-click events are assigned  $-1$  for  $B_1, B_2, A_1, A_2$ , but are assigned  $0$  for  $A_0$ .

3. **Parameter Estimation.** Alice and Bob communicate to estimate the CHSH score,

$$S(\eta, F) \equiv \langle A_1(B_1 + B_2) \rangle + \langle A_2(B_1 - B_2) \rangle \quad (14)$$

4. **Privacy Amplification.** Alice uses measurement results  $A_0$  to infer Bob’s key  $B_1$  using hash function techniques based on the value of  $S$  to minimize the information that might leak and maximize the correctness of the key.

Then, the key rate per single use of the channel can be calculated as [54]

$$r_{\text{DI-QKD}}(\eta, F) \geq 1 - h \left( \frac{1 + \sqrt{(S/2)^2 - 1}}{2} \right) - H(B_1|A_0), \quad (15)$$

where  $h(x) = -x \log x - (1-x) \log(1-x)$  is the binary entropy function. The total key rate is given by integrating over the linewidth of the channels as

$$R_{\text{DI-QKD}} = \int r_{\text{DI-QKD}} d\nu \approx r_{\text{DI-QKD}}(\eta, F) \Delta\nu, \quad (16)$$

which has a unit of bits per second.

The achievable key rate for performing the DI-QKD protocol mentioned above, with a growing transmission distance, is shown with different generation fidelity in Fig. 4. With the achievable parameters  $F = 0.99$ , it demonstrates a Terabit/second key rate over a continental distance of  $10^4$ km, which can be further improved with a more advanced protocol. As DI-QKD protocols base their security on the test of Bell-like inequalities, a practical scheme for DI-QKD also implies the feasibility of the fundamental and loophole-free test for Bell inequality [88].

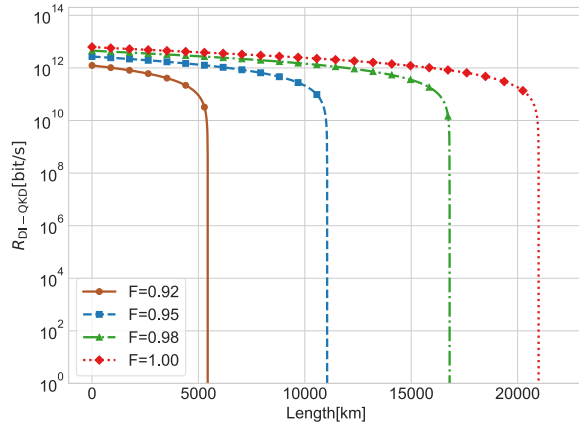


FIG. 4. DI-QKD key rate vs transmission distances using VBG channel with different fidelities at generation.

## B. Long Base-line Quantum Telescope

A Quantum Telescope (QTelescope) with a long base-line was proposed and theoretically shown to have quadratic precision enhancement in terms of source brightness  $\varepsilon$  for the angle measurement of faint stellar objects that can be effectively treated as weak thermal sources [89]. The illustration of a basic model for a double-receiver long baseline quantum telescope [68–70] is shown in Fig. 5(a), where the incoming stellar light from both receivers is combined via the quantum channel to generate an interference pattern with a phase shift  $\phi_0$ , revealing the incoming angle information via  $\phi_0 = \frac{2\pi L}{\lambda} \sin \theta$ , with  $L$  being the baseline distance. The quantum telescope offers benefits over classical local schemes due to its ability to remove the position information of incoming photons by projecting out the vacuum state,

thereby reducing uncertainty in momentum according to Heisenberg’s principle.

To quantitatively describe the performance of VBG, we estimate the uncertainty of  $\theta$  in a single measurement with a time window  $\tau$  for integration, which can be related to the uncertainty of  $\phi_0$  via the following simple error synthesis formula,

$$\sigma_\theta = \frac{\lambda}{2\pi L |\cos \theta|} \sigma_{\phi_0}, \quad (17)$$

In the direct interference scheme,  $\phi_0$  is encoded in the following state that describes the incoming photon upon detection:

$$\rho_s = (1 - \varepsilon\eta)|00\rangle\langle 00| + \frac{\eta\varepsilon}{2} [|01\rangle\langle 01| + g e^{-\frac{1}{2}\sigma_\phi^2} e^{i\phi_0} |01\rangle\langle 10| + h.c.], \quad (18)$$

where  $\eta$  is again the transmission efficiency;  $\sigma_\phi^2 \equiv \gamma L$  is the average dephasing in the transmission;  $g$  is the first-order correlation strength; and  $\varepsilon$  is the probability of containing a single photon from the incoming stellar wave packet. Fisher information [90] can be employed to estimate the lower bound of the uncertainty using the corresponding POVM optimized photon detection over delay  $\delta$  as

$$(\delta\theta \cdot |g| \cos \theta)^2 \geq \frac{\lambda^2}{4\pi^2 L^2} \frac{|g|}{F(\phi_0, \delta)} = A(\varepsilon, \lambda) \times \frac{e^{(\gamma+0.5\alpha)L}}{L^2}, \quad (19)$$

where  $A(\varepsilon, \lambda) = \frac{\lambda^2}{4\pi^2 \varepsilon}$  is a pre-factor that depends on the source.

If there are no geographical constraints, the above equation reaches its minimum at  $L = \frac{2}{\gamma+0.5\alpha}$  with a minimum value  $\frac{\lambda^2 e^{2(0.5\alpha+\gamma)}}{16\pi^2 \varepsilon}$ . For an example calculation, let  $\tau \approx 0.01$ s be the atmosphere coherence time [91].  $\alpha$  can be computed from Eq. (4) via a simple unit conversion;  $\varepsilon \approx \frac{\tau}{1\text{s}} \approx 0.01$  for a stellar source in the H band with a magnitude of 24, which is the limiting magnitude of automated allsky astronomical surveys [92]; and  $\gamma \approx 2 \int_0^{1/\tau} \hat{S}_\phi(f) = 3.6 \times 10^{-10} \text{rad}^2/\text{km}$ , which is negligible compared to attenuation.

The precision of the VBG scheme versus different baseline lengths, compared to the fiber scheme, is plotted in Fig. 5(b) for comparison, which demonstrates a clear advantage of the VBG channel. At a scale of 1000km, the quantum telescopes can reach a precision approaching the micro-arcsecond level. However, the optimal baseline length is beyond  $10^4$ km, where the main limitation will be the Earth’s curvature.

## C. Blind Delegated Quantum Computation

For delegating quantum computing tasks to the cloud, clients can transmit the entire quantum circuit and fetch outcomes using solely classical communication, provided

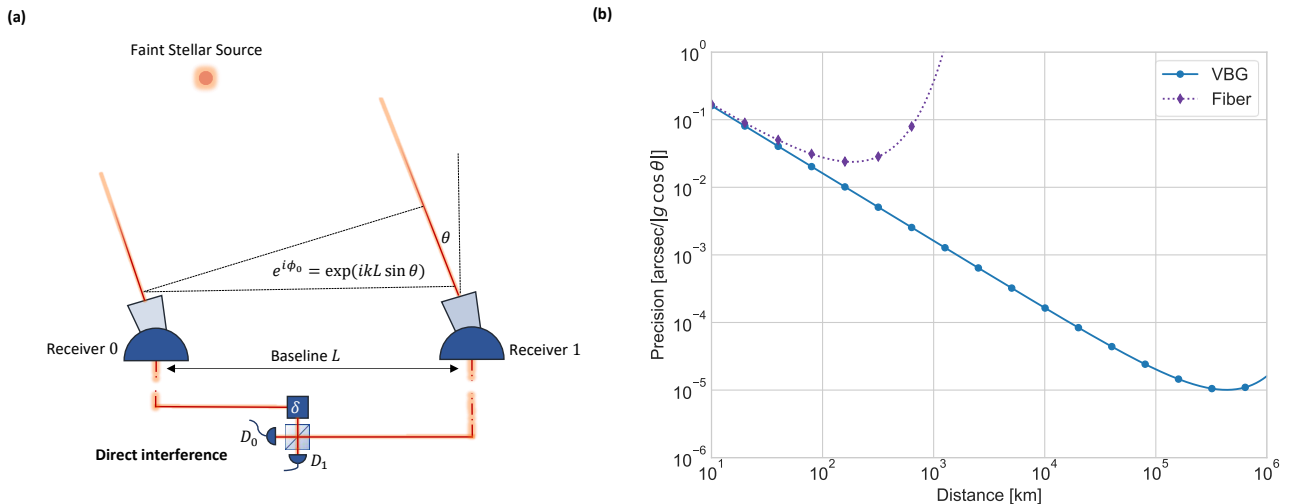


FIG. 5. Illustration and performance of Q-Telescope. (a) The light from both telescope stations are directly interfered to eliminate the position information.  $D_i$  is the photon detector. (b) Precision bounded by Fisher information versus baseline, assuming different schemes for an H-band magnitude 24 stellar object under a single atmosphere coherent period.

that both input and output are classical. Nevertheless, when computations involve sensitive data or commercial confidentiality, clients may wish to conceal this information from the server while still utilizing its quantum capabilities. This situation introduces blind quantum computation (BQC) [79]. Two principal strategies exist for achieving BQC: The pioneering universal BQC protocol [93] involves clients obfuscating their commands to ensure that only the circuit size can be leaked; Quantum private query techniques can be applied to include decoy instructions, thereby identifying deceitful servers with high certainty [94]. This discussion will concentrate on the first method, which ingeniously leverages measurement-based quantum computation (MBQC).

The primary aim is to achieve private quantum computation for a classical client. However, existing methods still require the client to perform at least some basic quantum operations, as fully classical clients with a single quantum server imply a non-trivial connection between BQP and NP. If clients can conduct arbitrary single-qubit measurements, the protocol becomes remarkably simple yet highly secure [80]: The client simply asks the server to prepare the required resource state for MBQC. The qubits are then sent to the client for adaptive measurement. Throughout this process, the client ensures that no computational details are exposed due to the no-signal theorem [95]. Despite the significant advantages, its main limitation is its vulnerability to loss. Consider a quantum circuit using an  $M$ -qubit resource state executed with a single-qubit coupling efficiency  $\eta$ ; the worst-case success probability is  $P_{\text{success}} = \eta^M$ . Although VBG can achieve high coupling efficiency over continental distances, the growth of circuit size is still hindered by exponential decay, as illustrated in Fig. 6. The fiber can only support a

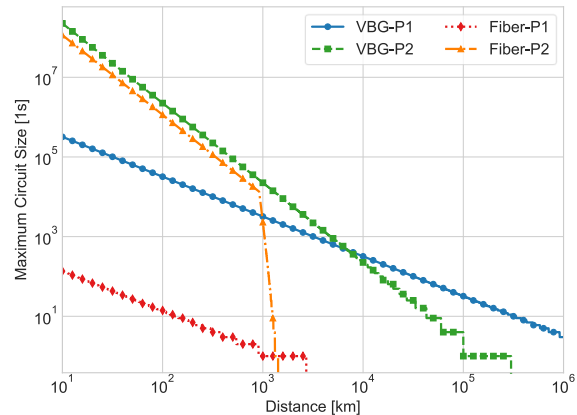


FIG. 6. The maximum circuit size assuming linear depth scaling that can be executed within one second versus distance between server and client under the direct measurement protocol and the heralded Bell pair protocol.

circuit size of 10 qubits at an urban scale. In comparison, computations involving  $10^4$  qubits across thousands of kilometers are feasible with VBG, exceeding the current limit of local quantum computation. Thus, transmission loss might not be the main limitation. Moreover, quantum error correction techniques, standard in quantum computing [96, 97], can mitigate the exponential decay of the success probability.

Another possible solution [80] is to utilize quantum teleportation with heralding, where the server sends half of the Bell pair to the client and requires the client to acknowledge receipt. In particular, the client can im-

mediately perform the necessary measurement once the bell pair is successfully received, without forwarding the measurement results to the server. This eliminates the requirement for quantum memory, as in the previous case. Therefore, the expected number of sent qubits from the server now scales as  $\frac{M}{\eta}$ . However, this protocol requires QND techniques to herald [98] and sacrifices some security for the sake of loss tolerance, as extra communication between the server and the client may allow for a storage attack [99]. Another serious issue is that the execution time of a depth  $d$  will now be limited by the communication time  $\tau_r = L/c$  between them. Assuming that the resources are properly allocated so that at least one Bell pair is established for each qubit in a single round, the minimum execution time is limited by  $\max\left(\frac{N}{\eta R_B}, \tau_c\right)d$ , where  $R_B$  is the maximum Bell pair transmission rate under ideal multiplexing, and  $N$  is the number of qubits in a single layer. This is because the measurement results of the previous layer of the circuit from the server still need to be fed into the next layer and cannot be executed in parallel. The performance of this protocol under VBG, assuming linear depth growth, is also shown in Fig. 6 compared to the previous one. Although the heralded protocol is free from exponential decay and thus performs better than the previous one on a continental scale, one does observe that the former gains advantages when the communication delay is significant. This disadvantage will become more pronounced when the depth of the circuit establishes super-linear scaling, which is common in fault-tolerant quantum computation [100, 101].

#### IV. DISCUSSION

In this work, we construct a comprehensive and detailed model of the VBG channel for bosonic quantum information. A more detailed description of channel loss and linewidth is based on previous work [10], taking into account the curvature of the Earth and possible reflective configurations to circumvent it. We also derive the full phase noise power spectral density characterizing the interference stability of the VBG channel, quantitatively referring to the realistic parameters and experimental performance of the LIGO system [24, 102], which shows an rms phase noise of  $10^{-6}\text{rad}/\sqrt{\text{km} \cdot \text{Hz}}$  after active subtraction. In addition, we describe the robustness of the VBG polarization using the Kraus operators that correspond to a mixture of phase shift and bit flip errors under polarization encoding, with a probability of only 1ppm per section. Finally, the transmission delay and wave packet spreading due to dispersion effects are also estimated, assuming the LIGO optics [46], which are considered essential for relativistic-related applications.

Theoretical and numerical analyses reveal substantial enhancements in the performance of a wide range of quantum protocols when implementing VBG. Within the field of secure quantum communication, VBG facili-

tates the operation of extant QPV and DI-QKD protocols using current technological capabilities by ensuring that the channel attenuation remains below the threshold prescribed by these protocols across continental distances. Furthermore, the capacity of VBG to transmit quantum signals with high fidelity between widely separated detectors enables it to achieve an unparalleled level of precision in applications such as quantum telescopes, clock synchronization, and other potential distributed sensing tasks. The realm of network quantum computation reaps considerable benefits from the robust establishment of quantum entanglement: a straightforward direct measurement protocol allows for the execution of blind delegated quantum computations over distances extending to thousands of kilometers, with circuits comprising more than  $10^3$  qubits; additionally, quantum-enhanced high-frequency trading offers demonstrable advantages for traders situated on different continents.

In parallel with the development of the comprehensive and analytical model in this study, intricate simulations utilizing Finesse3 or comparable optical software packages [103, 104] are being executed to offer a more precise depiction and to rigorously assess the efficacy of VBG systems. Given that VBG is anticipated to extend over a continental span, it is crucial to incorporate transient, albeit significant, environmental disturbances into the analysis to assure ample redundancy that guarantees longevity and robustness in operational cycles. Although these noises have been preliminarily estimated in Appendix.B 5, such estimations merely provide orders of magnitude and underscore the necessity for more precise simulations capable of capturing the intricate dynamics and interdependence of these noise variables. Despite this, the most straightforward method for evaluating performance is to implement the system at full scale and obtain empirical data following methods analogous to those employed by LIGO [105, 106]. To some extent, LIGO itself serves as a conceptual validation for the VBG system, though with modifications, since the anticipated demands for the VBG system entail more relaxed constraints to mitigate costs. Notably, small-scale experimentation using earlier LIGO experimental tubes [107] is feasible and is currently under active exploration.

Beyond the applications proposed and analyzed in the primary text, VBG can be integrated with all-photonics repeaters [108, 109] to establish a quantum network that theoretically possesses an unlimited scale, facilitating the execution of a Bell test experiment with cognitive observers to examine the basic measurement assumption [110] or to perform quantum holographic tasks [111]. We anticipate that VBG will offer universal enhancement and serve as a robust, expansive experimental platform, significantly impacting not only future quantum technologies but also providing cross-disciplinary advantages: facilitating the long-range transmission of light bullets [112, 113]; directly interlinking multiple LIGO detectors, which may become the central component of the anticipated Einstein telescope [114]; and extending worldwide

to perform large-scale geodesy measurements [115]. Our VBG model, as presented, lays a solid groundwork for implementation and advocates for imminent construction efforts, potentially bringing about extensive multidisciplinary benefits.

## ACKNOWLEDGMENTS

We thank J.C Diels, Ming Lai, Ming Li, Kaushik Seshadreesan, Allen Zang, and Haiqi Zhou for their helpful discussions. This paper describes objective technical results and analysis. This research is supported by ARO(W911NF-23-1-0077), ARO MURI (W911NF-21-1-0325), AFOSR MURI (FA9550-19-1-0399, FA9550-21-1-0209, FA9550-23-1-0338), DARPA (HR0011-24-9-0359, HR0011-24-9-0361), NSF (OMA-1936118, ERC-1941583,

OMA-2137642, OSI-2326767, CCF-2312755), NTT Research, Packard Foundation (2020-71479), and the Marshall and Arlene Bennett Family Research Program. U.S. Department of Energy, Office of Science, National Quantum Information Science Research Centers and Advanced Scientific Computing Research (ASCR) program (DE-AC02-06CH11357) and Oak Ridge Leadership Computing Facility (DE-AC05-00OR22725). National Science Foundation (Grant No. DMS-1929348). University of Pittsburgh, School of Computing and Information, Department of Computer Science, Pitt Cyber, Pitt Momentum Fund, PQI Community Collaboration Awards, John C. Mascaró Faculty Scholar in Sustainability, and Cisco Research. Any subjective views or opinions that might be expressed in the paper do not necessarily represent the views of the U.S. Department of Energy or the United States Government.

- 
- [1] M. Petrovich, E. N. Fokoua, Y. Chen, H. Sakr, A. I. Adamu, R. Hassan, D. Wu, R. F. Ando, A. Papadimopoulos, S. R. Sandoghchi, *et al.*, First broadband optical fibre with an attenuation lower than 0.1 decibel per kilometre, arXiv preprint arXiv:2503.21467 (2025).
- [2] E. Numkam Fokoua, S. Abokhamis Mousavi, G. T. Jasion, D. J. Richardson, and F. Poletti, Loss in hollow-core optical fibers: mechanisms, scaling rules, and limits, *Advances in Optics and Photonics* **15**, 1 (2023).
- [3] H. Sakr, T. D. Bradley, G. T. Jasion, E. N. Fokoua, S. R. Sandoghchi, I. A. Davidson, A. Taranta, G. Guerra, W. Shere, Y. Chen, *et al.*, Hollow core nanfs with five nested tubes and record low loss at 850, 1060, 1300 and 1625nm, in *Optical Fiber Communication Conference* (Optica Publishing Group, 2021) pp. F3A–4.
- [4] M. Aspelmeyer, H. R. Bohm, T. Gyatso, T. Jennewein, R. Kaltenbaek, M. Lindenthal, G. Molina-Terriza, A. Poppe, K. Resch, M. Taraba, *et al.*, Long-distance free-space distribution of quantum entanglement, *science* **301**, 621 (2003).
- [5] C.-Y. Lu, Y. Cao, C.-Z. Peng, and J.-W. Pan, Micius quantum experiments in space, *Reviews of Modern Physics* **94**, 035001 (2022).
- [6] S. Goswami and S. Dhara, Satellite-relayed global quantum communication without quantum memory, *Physical Review Applied* **20**, 024048 (2023).
- [7] J. Yin, Y. Cao, Y.-H. Li, S.-K. Liao, L. Zhang, J.-G. Ren, W.-Q. Cai, W.-Y. Liu, B. Li, H. Dai, *et al.*, Satellite-based entanglement distribution over 1200 kilometers, *Science* **356**, 1140 (2017).
- [8] S.-K. Liao, W.-Q. Cai, W.-Y. Liu, L. Zhang, Y. Li, J.-G. Ren, J. Yin, Q. Shen, Y. Cao, Z.-P. Li, *et al.*, Satellite-to-ground quantum key distribution, *Nature* **549**, 43 (2017).
- [9] S. Muralidharan, L. Li, J. Kim, N. Lütkenhaus, M. D. Lukin, and L. Jiang, Optimal architectures for long distance quantum communication, *Scientific reports* **6**, 20463 (2016).
- [10] Y. Huang, F. Salces-Carcoba, R. X. Adhikari, A. H. Safavi-Naeini, and L. Jiang, Vacuum beam guide for large scale quantum networks, *Physical Review Letters* **133**, 020801 (2024).
- [11] A. S. Holevo and R. F. Werner, Evaluating capacities of bosonic gaussian channels, *Physical Review A* **63**, 032312 (2001).
- [12] K. Noh, V. V. Albert, and L. Jiang, Quantum capacity bounds of gaussian thermal loss channels and achievable rates with Gottesman-Kitaev-Preskill codes, *IEEE Transactions on Information Theory* **65**, 2563 (2018).
- [13] C.-H. Wang, F. Li, and L. Jiang, Quantum capacities of transducers, *Nature Communications* **13**, 6698 (2022).
- [14] M. Takeoka, S. Guha, and M. M. Wilde, Fundamental rate-loss tradeoff for optical quantum key distribution, *Nature communications* **5**, 5235 (2014).
- [15] P. Leviant, Q. Xu, L. Jiang, and S. Rosenblum, Quantum capacity and codes for the bosonic loss-dephasing channel, *Quantum* **6**, 821 (2022).
- [16] G. Zheng, W. He, G. Lee, K. Noh, and L. Jiang, Performance and achievable rates of the Gottesman-Kitaev-Preskill code for pure-loss and amplification channels, arXiv preprint arXiv:2412.06715 (2024).
- [17] Y. Zhang and T. Jennewein, Criteria for optimal entanglement-assisted long baseline imaging protocols, arXiv preprint arXiv:2501.16670 (2025).
- [18] S. D. Bartlett, T. Rudolph, and R. W. Spekkens, Reference frames, superselection rules, and quantum information, *Reviews of Modern Physics* **79**, 555 (2007).
- [19] W. J. Riley and D. A. Howe, *Handbook of frequency stability analysis*, Vol. 1065 (US Department of Commerce, National Institute of Standards and Technology . . . , 2008).
- [20] W. P. Robins, *Phase noise in signal sources: theory and applications*, Vol. 9 (IET, 1984).
- [21] D. V. Martynov, E. Hall, B. Abbott, R. Abbott, T. Abbott, C. Adams, R. Adhikari, R. Anderson, S. Anderson, K. Arai, *et al.*, Sensitivity of the advanced LIGO detectors at the beginning of gravitational wave astronomy, *Physical Review D* **93**, 112004 (2016).
- [22] A. Buikema, C. Cahillane, G. Mansell, C. Blair, R. Abbott, C. Adams, R. Adhikari, A. Ananyeva, S. Appert, K. Arai, *et al.*, Sensitivity and performance of the advanced LIGO detectors in the third observing run, *Physi-*

- cal Review D **102**, 062003 (2020).
- [23] E. Capote, W. Jia, N. Aritomi, M. Nakano, V. Xu, R. Abbott, I. Abouelfettouh, R. Adhikari, A. Ananyeva, S. Appert, *et al.*, Advanced ligo detector performance in the fourth observing run, *Physical Review D* **111**, 062002 (2025).
- [24] J. Aasi, B. Abbott, R. Abbott, T. Abbott, M. Abernathy, K. Ackley, C. Adams, T. Adams, P. Addesso, R. Adhikari, *et al.*, Advanced ligo, *Classical and quantum gravity* **32**, 074001 (2015).
- [25] S. Pirandola, R. Laurenza, C. Ottaviani, and L. Banchi, Fundamental limits of repeaterless quantum communications, *Nature communications* **8**, 15043 (2017).
- [26] G. Zheng, W. He, G. Lee, K. Noh, and L. Jiang, Performance and achievable rates of the Gottesman-Kitaev-Preskill code for pure-loss and amplification channels, *PRX Quantum* **6**, 030314 (2025).
- [27] D. Gottesman, A. Kitaev, and J. Preskill, Encoding a qubit in an oscillator, *Physical Review A* **64**, 012310 (2001).
- [28] A. L. Grimsmo and S. Puri, Quantum error correction with the Gottesman-Kitaev-Preskill code, *PRX Quantum* **2**, 020101 (2021).
- [29] M. Subramanian, G. Zheng, and L. Jiang, Achievable rates for concatenated square Gottesman-Kitaev-Preskill codes, *arXiv preprint arXiv:2505.10499* (2025).
- [30] M. Lucamarini, Z. L. Yuan, J. F. Dynes, and A. J. Shields, Overcoming the rate-distance limit of quantum key distribution without quantum repeaters, *Nature* **557**, 400 (2018).
- [31] M. Sandfuchs, M. Haberland, V. Vilasini, and R. Wolf, Security of differential phase shift QKD from relativistic principles, *Quantum* **9**, 1611 (2025).
- [32] S. Wang, Z.-Q. Yin, D.-Y. He, W. Chen, R.-Q. Wang, P. Ye, Y. Zhou, G.-J. Fan-Yuan, F.-X. Wang, W. Chen, *et al.*, Twin-field quantum key distribution over 830-km fibre, *Nature Photonics* **16**, 154 (2022).
- [33] Y. Mao, P. Zeng, and T.-Y. Chen, Recent advances on quantum key distribution overcoming the linear secret key capacity bound, *Advanced Quantum Technologies* **4**, 2000084 (2021).
- [34] R. Nehra, C. Oh, L. Jiang, and A. Marandi, All-optical loss-tolerant distributed quantum sensing, *arXiv preprint arXiv:2407.13654* (2024).
- [35] A. Zang, A. Kolar, A. Gonzales, J. Chung, S. K. Gray, R. Kettimuthu, T. Zhong, and Z. H. Saleem, Quantum advantage in distributed sensing with noisy quantum networks, *arXiv preprint arXiv:2409.17089* (2024).
- [36] S. M. Foreman, K. W. Holman, D. D. Hudson, D. J. Jones, and J. Ye, Remote transfer of ultrastable frequency references via fiber networks, *Review of Scientific Instruments* **78** (2007).
- [37] D. Shoemaker *et al.*, Advanced ligo reference design, *LIGO Report* **60056** (2009).
- [38] M. Evans, P. Fritschel, D. McClelland, J. Miller, A. Mullavey, D. Shaddock, B. Slagmolen, S. Waldman, *et al.*, Advanced ligo arm length stabilisation system design, *LIGO Report* **900144** (2009).
- [39] R. Abbott, R. Adhikari, G. Allen, S. Cowley, E. Daw, D. DeBra, J. Giaime, G. Hammond, M. Hammond, C. Hardham, *et al.*, Seismic isolation for advanced ligo, *Classical and Quantum Gravity* **19**, 1591 (2002).
- [40] F. Matichard, B. Lantz, R. Mittleman, K. Mason, J. Kissel, B. Abbott, S. Biscans, J. McIver, R. Abbott, S. Abbott, *et al.*, Seismic isolation of advanced ligo: Review of strategy, instrumentation and performance, *Classical and Quantum Gravity* **32**, 185003 (2015).
- [41] R. E. Bartolo, A. B. Tveten, and A. Dandridge, Thermal phase noise measurements in optical fiber interferometers, *IEEE Journal of Quantum Electronics* **48**, 720 (2012).
- [42] K. H. Wanser, Fundamental phase noise limit in optical fibres due to temperature fluctuations, *Electronics Letters* **28**, 53 (1992).
- [43] L. Duan, Intrinsic thermal noise of optical fibres due to mechanical dissipation, *Electronics Letters* **46**, 1515 (2010).
- [44] Y. Michimura, H. Wang, F. Salces-Carcoba, C. Wipf, A. Brooks, K. Arai, and R. X. Adhikari, Effects of mirror birefringence and its fluctuations to laser interferometric gravitational wave detectors, *Physical Review D* **109**, 022009 (2024).
- [45] E. Hirose, G. Billingsley, L. Zhang, H. Yamamoto, L. Pinard, C. Michel, D. Forest, B. Reichman, and M. Gross, Characterization of core optics in gravitational-wave detectors: Case study of kagra sapphire mirrors, *Physical Review Applied* **14**, 014021 (2020).
- [46] L. Pinard, C. Michel, B. Sassolas, L. Balzarini, J. Degallaix, V. Dolique, R. Flaminio, D. Forest, M. Granata, B. Lagrange, *et al.*, Mirrors used in the ligo interferometers for first detection of gravitational waves, *Applied Optics* **56**, C11 (2017).
- [47] J.-C. Diels and W. Rudolph, *Ultrashort laser pulse phenomena* (Elsevier, 2006).
- [48] Y. Arosa and R. de la Fuente, Refractive index spectroscopy and material dispersion in fused silica glass, *Optics Letters* **45**, 4268 (2020).
- [49] A. K. Ekert, Quantum cryptography based on Bell's theorem, *Physical Review Letters* **67**, 661 (1991).
- [50] A. Acín, N. Brunner, N. Gisin, S. Massar, S. Pironio, and V. Scarani, Device-independent security of quantum cryptography against collective attacks, *Physical Review Letters* **98**, 230501 (2007).
- [51] L. Masanes, S. Pironio, and A. Acín, Secure device-independent quantum key distribution with causally independent measurement devices, *Nature Communications* **2**, 238 (2011).
- [52] U. Vazirani and T. Vidick, Fully device independent quantum key distribution, *Communications of the ACM* **62**, 133 (2019).
- [53] R. Arnon-Friedman, F. Dupuis, O. Fawzi, R. Renner, and T. Vidick, Practical device-independent quantum cryptography via entropy accumulation, *Nature Communications* **9**, 459 (2018).
- [54] P. Sekatski, J.-D. Bancal, X. Valcarce, E. Y.-Z. Tan, R. Renner, and N. Sangouard, Device-independent quantum key distribution from generalized CHSH inequalities, *Quantum* **5**, 444 (2021).
- [55] W. Zhang, T. van Leent, K. Redeker, R. Garthoff, R. Schwonnek, F. Fertig, S. Eppelt, W. Rosenfeld, V. Scarani, C. C.-W. Lim, *et al.*, A device-independent quantum key distribution system for distant users, *Nature* **607**, 687 (2022).
- [56] F. Xu, Y.-Z. Zhang, Q. Zhang, and J.-W. Pan, Device-independent quantum key distribution with random postselection, *Physical Review Letters* **128**, 110506 (2022).

- [57] V. Zapatero, T. van Leent, R. Arnon-Friedman, W.-Z. Liu, Q. Zhang, H. Weinfurter, and M. Curty, Advances in device-independent quantum key distribution, *npj quantum information* **9**, 10 (2023).
- [58] K. Kravtsov, I. Radchenko, S. Kulik, and S. Molotkov, Relativistic quantum key distribution system with one-way quantum communication, *Scientific reports* **8**, 6102 (2018).
- [59] V. Giovannetti, S. Lloyd, and L. Maccone, Quantum private queries, *Physical review letters* **100**, 230502 (2008).
- [60] H. Buhrman, N. Chandran, S. Fehr, R. Gelles, V. Goyal, R. Ostrovsky, and C. Schaffner, Position-based quantum cryptography: Impossibility and constructions, *SIAM Journal on Computing* **43**, 150 (2014).
- [61] A. Bluhm, M. Christandl, and F. Speelman, A single-qubit position verification protocol that is secure against multi-qubit attacks, *Nature Physics* **18**, 623 (2022).
- [62] R. Allerstorfer, A. Bluhm, H. Buhrman, M. Christandl, L. Escolà-Farràs, F. Speelman, and P. V. Lunel, Making existing quantum position verification protocols secure against arbitrary transmission loss, *arXiv preprint arXiv:2312.12614* (2023).
- [63] A. Fischer and D. Towsley, Distributing graph states across quantum networks, in *2021 IEEE International Conference on Quantum Computing and Engineering (QCE)* (IEEE, 2021) pp. 324–333.
- [64] C. Meignant, D. Markham, and F. Grosshans, Distributing graph states over arbitrary quantum networks, *Physical Review A* **100**, 052333 (2019).
- [65] X. Fan, C. Zhan, H. Gupta, and C. Ramakrishnan, Optimized distribution of entanglement graph states in quantum networks, *IEEE Transactions on Quantum Engineering* (2025).
- [66] Y. Huang, X. Ren, B. Li, Y. Wong, Z. Liang, and L. Jiang, Peer-to-peer distribution of graph states across spacetime quantum networks of arbitrary topology, *Proceedings of the ACM on Measurement and Analysis of Computing Systems* **9**, 1 (2025).
- [67] X. Fan, Y. Yang, H. Gupta, and C. Ramakrishnan, Distribution and purification of entanglement states in quantum networks, in *2025 International Conference on Quantum Communications, Networking, and Computing (QCNC)* (IEEE, 2025) pp. 74–82.
- [68] E. T. Khabiboulline, J. Borregaard, K. De Greve, and M. D. Lukin, Quantum-assisted telescope arrays, *Physical review A* **100**, 022316 (2019).
- [69] E. T. Khabiboulline, J. Borregaard, K. De Greve, and M. D. Lukin, Optical interferometry with quantum networks, *Physical review letters* **123**, 070504 (2019).
- [70] D. Gottesman, T. Jennewein, and S. Croke, Long-baseline telescopes using quantum repeaters, *Physical review letters* **109**, 070503 (2012).
- [71] V. Giovannetti, S. Lloyd, and L. Maccone, Quantum-enhanced positioning and clock synchronization, *Nature* **412**, 417 (2001).
- [72] P. Komar, E. M. Kessler, M. Bishof, L. Jiang, A. S. Sørensen, J. Ye, and M. D. Lukin, A quantum network of clocks, *Nature Physics* **10**, 582 (2014).
- [73] V. Giovannetti, S. Lloyd, and L. Maccone, Positioning and clock synchronization through entanglement, *Physical Review A* **65**, 022309 (2002).
- [74] A. J. Brady and S. Haldar, Frame dragging and the hong-ou-mandel dip: Gravitational effects in multiphoton interference, *Physical Review Research* **3**, 023024 (2021).
- [75] F. Giovannetti, C. Altucci, F. Bajardi, A. Basti, N. Beverini, S. Capozziello, G. Carelli, S. Castellano, D. Ciampini, G. Di Somma, *et al.*, Gingerino: A high sensitivity ring laser gyroscope for fundamental and quantum physics investigation, *Frontiers in Quantum Science and Technology* **3**, 1363409 (2024).
- [76] A. D. Di Virgilio, F. Bajardi, A. Basti, N. Beverini, G. Carelli, D. Ciampini, G. Di Somma, F. Fuso, E. Maccioni, P. Marsili, *et al.*, Noise level of a ring laser gyroscope in the femto-rad/s range, *Physical Review Letters* **133**, 013601 (2024).
- [77] J. Liu, C. T. Hann, and L. Jiang, Data centers with quantum random access memory and quantum networks, *Physical Review A* **108**, 032610 (2023).
- [78] J. Liu and L. Jiang, Quantum data center: Perspectives, *IEEE Network* (2024).
- [79] J. F. Fitzsimons, Private quantum computation: an introduction to blind quantum computing and related protocols, *npj Quantum Information* **3**, 23 (2017).
- [80] T. Morimae and K. Fujii, Blind quantum computation protocol in which alice only makes measurements, *Physical Review A* **87**, 050301 (2013).
- [81] H. Buhrman, R. Cleve, S. Massar, and R. De Wolf, Nonlocality and communication complexity, *Reviews of modern physics* **82**, 665 (2010).
- [82] A. C.-C. Yao, Quantum circuit complexity, in *Proceedings of 1993 IEEE 34th Annual Foundations of Computer Science* (IEEE, 1993) pp. 352–361.
- [83] G. Brassard, Quantum communication complexity, *Foundations of Physics* **33**, 1593 (2003).
- [84] G. S. Ravi, K. N. Smith, P. Gokhale, and F. T. Chong, Quantum computing in the cloud: Analyzing job and machine characteristics, in *2021 IEEE International Symposium on Workload Characterization (IISWC)* (IEEE, 2021) pp. 39–50.
- [85] S. Wehner, D. Elkouss, and R. Hanson, Quantum internet: A vision for the road ahead, *Science* **362**, eaam9288 (2018).
- [86] S. J. Devitt, Performing quantum computing experiments in the cloud, *Physical Review A* **94**, 032329 (2016).
- [87] J.-Å. Larsson and J. Semitecolos, Strict detector-efficiency bounds for n-site clauser-horne inequalities, *Physical Review A* **63**, 022117 (2001).
- [88] M. Giustina, M. A. Versteegh, S. Wengerowsky, J. Handsteiner, A. Hochrainer, K. Phelan, F. Steinlechner, J. Kofler, J.-Å. Larsson, C. Abellán, *et al.*, A significant-loophole-free test of bell’s theorem with entangled photons, in *Quantum Information Science and Technology III*, Vol. 10442 (SPIE, 2017) pp. 19–27.
- [89] M. Tsang, Quantum nonlocality in weak-thermal-light interferometry, *Physical review letters* **107**, 270402 (2011).
- [90] B. R. Frieden and R. A. Gatenby, Principle of maximum fisher information from hardy’s axioms applied to statistical systems, *Physical Review E* **88**, 042144 (2013).
- [91] S. Lacour, F. Eisenhauer, S. Gillessen, O. Pfuhl, J. Woillez, H. Bonnet, G. Perrin, B. Lazareff, S. Rabien, V. Lapeyrere, *et al.*, Reaching micro-arcsecond astrometry with long baseline optical interferometry-application to the gravity instrument, *Astronomy & Astrophysics* **567**, A75 (2014).
- [92] N. Kaiser, H. Aussel, B. E. Burke, H. Boesgaard,

- K. Chambers, M. R. Chun, J. N. Heasley, K.-W. Hodapp, B. Hunt, R. Jedicke, *et al.*, Pan-starrs: a large synoptic survey telescope array, in *Survey and Other Telescope Technologies and Discoveries*, Vol. 4836 (SPIE, 2002) pp. 154–164.
- [93] A. Broadbent, J. Fitzsimons, and E. Kashefi, Universal blind quantum computation, in *2009 50th annual IEEE symposium on foundations of computer science* (IEEE, 2009) pp. 517–526.
- [94] V. Giovannetti, L. Maccone, T. Morimae, and T. G. Rudolph, Efficient universal blind quantum computation, *Physical review letters* **111**, 230501 (2013).
- [95] A. Peres and D. R. Terno, Quantum information and relativity theory, *Reviews of Modern Physics* **76**, 93 (2004).
- [96] S. D. Barrett and T. M. Stace, Fault tolerant quantum computation with very high threshold for loss errors, *Physical review letters* **105**, 200502 (2010).
- [97] Q. Xu, J. P. Bonilla Ataides, C. A. Pattison, N. Raveendran, D. Bluvstein, J. Wurtz, B. Vasić, M. D. Lukin, L. Jiang, and H. Zhou, Constant-overhead fault-tolerant quantum computation with reconfigurable atom arrays, *Nature Physics* **20**, 1084 (2024).
- [98] K. Xia, M. Johnsson, P. L. Knight, and J. Twamley, Cavity-free scheme for nondestructive detection of a single optical photon, *Physical review letters* **116**, 023601 (2016).
- [99] J. Barrett, R. Colbeck, and A. Kent, Memory attacks on device-independent quantum cryptography, *Physical review letters* **110**, 010503 (2013).
- [100] H. Yamasaki and M. Koashi, Time-efficient constant-space-overhead fault-tolerant quantum computation, *Nature Physics* **20**, 247 (2024).
- [101] S. Tamiya, M. Koashi, and H. Yamasaki, Polylog-time-and constant-space-overhead fault-tolerant quantum computation with quantum low-density parity-check codes, arXiv preprint arXiv:2411.03683 (2024).
- [102] B. Abbott, R. Abbott, R. Adhikari, P. Ajith, B. Allen, G. Allen, R. Amin, S. Anderson, W. Anderson, M. Arain, *et al.*, Ligo: the laser interferometer gravitational-wave observatory, *Reports on Progress in physics* **72**, 076901 (2009).
- [103] P. Maheshwari, Ligo surf 2024: Interim report ii—vacuum beam guide for quantum communication, LIGO Report (2024).
- [104] H. Rose, Analysis of a vacuum beam guide for quantum communications, LIGO Report (2024).
- [105] P. Nguyen, R. Schofield, A. Effler, C. Austin, V. Adya, M. Ball, S. Banagiri, K. Banowetz, C. Billman, C. Blair, *et al.*, Environmental noise in advanced ligo detectors, *Classical and Quantum Gravity* **38**, 145001 (2021).
- [106] J. Kruk and R. Schofield, Environmental monitoring: Coupling function calculator (2016).
- [107] F. J. Raab, Overview of ligo instrumentation, in *Gravitational Wave and Particle Astrophysics Detectors*, Vol. 5500 (SPIE, 2004) pp. 11–24.
- [108] K. Azuma, K. Tamaki, and H.-K. Lo, All-photonic quantum repeaters, *Nature communications* **6**, 1 (2015).
- [109] Y. Gan, M. Azari, N. K. Chandra, X. Jin, J. Cheng, K. P. Seshadreesan, and J. Liu, Quantum repeaters enhanced by vacuum beam guides, arXiv preprint arXiv:2504.13397 (2025).
- [110] J. S. Bell, *Speakable and unspeakable in quantum mechanics: Collected papers on quantum philosophy* (Cambridge university press, 2004).
- [111] A. May, Quantum tasks in holography, *Journal of High Energy Physics* **2019**, 1 (2019).
- [112] C. Guo, M. Xiao, M. Orenstein, and S. Fan, Structured 3d linear space–time light bullets by nonlocal nanophotonics, *Light: Science & Applications* **10**, 160 (2021).
- [113] A. Chong, W. H. Renninger, D. N. Christodoulides, and F. W. Wise, Airy–bessel wave packets as versatile linear light bullets, *Nature photonics* **4**, 103 (2010).
- [114] S. Kroker and R. Nawrodt, The einstein telescope, in *2014 IEEE Metrology for Aerospace (MetroAeroSpace)* (IEEE, 2014) pp. 288–292.
- [115] J. Li, E. Biondi, E. R. Heimisson, S. Puel, Q. Zhai, S. Zhang, V. Hjörleifsdóttir, X. Wei, E. Bird, A. Klesh, *et al.*, Minute-scale dynamics of recurrent dike intrusions in iceland with fiber-optic geodesy, *Science* **388**, 1189 (2025).
- [116] J. W. Goodman, *Introduction to Fourier optics* (Roberts and Company publishers, 2005).
- [117] G. Mueller, Beam jitter coupling in advanced ligo, *Optics Express* **13**, 7118 (2005).
- [118] B. Canuel, E. Genin, M. Mantovani, J. Marque, P. Ruggi, and M. Tacca, Sub-nanoradiant beam pointing monitoring and stabilization system for controlling input beam jitter in gravitational wave interferometers, *Applied Optics* **53**, 2906 (2014).
- [119] L. Barsotti, M. Evans, and P. Fritschel, Alignment sensing and control in advanced ligo, *Classical and Quantum Gravity* **27**, 084026 (2010).
- [120] F. Smolka, T. Brown, and H. Hill, Corner cube interferometer using extended sources, *Applied Optics* **15**, 2423 (1976).
- [121] J. J. Degnan, A tutorial on retroreflectors and arrays used in satellite and lunar laser ranging, in *Photonics*, Vol. 10 (MDPI, 2023) p. 1215.
- [122] R. Wagner, E. Speyerer, K. Burns, J. Danton, and M. Robinson, Revised coordinates for apollo hardware, *The International Archives of the Photogrammetry, Remote Sensing and Spatial Information Sciences* **39**, 517 (2012).
- [123] J. Hough, S. Rowan, and B. S. Sathyaprakash, The search for gravitational waves, *Journal of Physics B: Atomic, Molecular and Optical Physics* **38**, S497 (2005).
- [124] M. P. Ross, K. Venkateswara, C. Mow-Lowry, S. Cooper, J. Warner, B. Lantz, J. Kissel, H. Radkins, T. Shaffer, R. Mittleman, *et al.*, Towards windproofing ligo: reducing the effect of wind-driven floor tilt by using rotation sensors in active seismic isolation, *Classical and Quantum Gravity* **37**, 185018 (2020).
- [125] P. M. Shearer, *Introduction to seismology* (Cambridge university press, 2019).
- [126] R. Soomro, C. Weidle, L. Cristiano, S. Lebedev, T. Meier, and P. W. Group, Phase velocities of rayleigh and love waves in central and northern europe from automated, broad-band, interstation measurements, *Geophysical Journal International* **204**, 517 (2016).
- [127] D. Thomas, V. Mohit, and C. Christophe, Complementary filters shaping using  $\mathcal{H}_\infty$  synthesis, in *2019 7th International Conference on Control, Mechatronics and Automation (ICCMA)* (IEEE, 2019) pp. 459–464.
- [128] C. M. Harris and A. G. Piersol, *Harris’ shock and vibration handbook*, Vol. 5 (McGraw-Hill New York, 2002).
- [129] A. Downey and L. Micheli, *Vibration mechanics: A practical introduction for mechanical, civil, and*

- aerospace engineers, OSF (2025).
- [130] T. L. Schmitz and K. S. Smith, *Mechanical vibrations* (Springer, 2012).
- [131] J. Giaime, B. Lantz, C. Hardham, W. Hua, R. Adhikari, D. DeBra, G. Hammond, M. Hammond, J. How, S. Richman, *et al.*, Advanced ligo seismic isolation system conceptual design, LIGO document E **10016** (2001).
- [132] D. W. Allan, Should the classical variance be used as a basic measure in standards metrology?, *IEEE Transactions on instrumentation and measurement*, 646 (2012).
- [133] B. Lenoir, Predicting the variance of a measurement with 1/f noise, *Fluctuation and Noise Letters* **12**, 1350006 (2013).
- [134] Minus K Technology, Transmissibility curves for vibration isolation tables, platforms, isolators & systems: Performance (n.d.), section “BM-1 Isolator”.
- [135] N. A. Robertson, J. Hough, and L. S. Collaboration, Gas damping in advanced ligo suspensions, LIGO Document: LIGO-T0900416-v2 (2009).
- [136] R. Weiss, Mitscattering by residual gas [https://dcc.ligo.org/public/0028/t890025/001\\_T890025-01.pdf](https://dcc.ligo.org/public/0028/t890025/001_T890025-01.pdf) (1989).
- [137] G. M. Harry, A. M. Gretarsson, P. R. Saulson, S. E. Kittelberger, S. D. Penn, W. J. Startin, S. Rowan, M. M. Fejer, D. Crooks, G. Cagnoli, *et al.*, Thermal noise in interferometric gravitational wave detectors due to dielectric optical coatings, *Classical and Quantum Gravity* **19**, 897 (2002).
- [138] A. Amato, G. Cagnoli, M. Granata, B. Sassolas, J. Degallaix, D. Forest, C. Michel, L. Pinard, N. Demos, S. Gras, *et al.*, Optical and mechanical properties of ion-beam-sputtered nb 2 o 5 and tio 2-nb 2 o 5 thin films for gravitational-wave interferometers and an improved measurement of coating thermal noise in advanced ligo, *Physical Review D* **103**, 072001 (2021).
- [139] K. Somiya, Thermal noise of geo’s beamsplitter, LIGO Report (2009).
- [140] M. Evans, S. Ballmer, M. Fejer, P. Fritschel, G. Harry, and G. Ogin, Thermo-optic noise in coated mirrors for high-precision optical measurements, *Physical Review D* **78**, 102003 (2008).
- [141] J. Steinlechner, I. W. Martin, J. Hough, C. Krüger, S. Rowan, and R. Schnabel, Thermal noise reduction and absorption optimization via multimaterial coatings, *Physical Review D* **91**, 042001 (2015).
- [142] S. Dwyer and S. W. Ballmer, Radiative thermal noise for transmissive optics in gravitational-wave detectors, *Physical Review D* **90**, 043013 (2014).
- [143] B. Benthem and Y. Levin, Thermorefractive and thermochemical noise in the beamsplitter of the geo600 gravitational-wave interferometer, *Physical Review D* **80**, 062004 (2009).
- [144] F. Bielsa, A. Dupays, M. Fouché, R. Battesti, C. Robilliard, and C. Rizzo, Birefringence of interferential mirrors at normal incidence: Experimental and computational study, *Applied Physics B* **97**, 457 (2009).
- [145] M. Kitagawa and M. Tateda, Form birefringence of sio<sub>2</sub>/ta<sub>2</sub>o<sub>5</sub> periodic multilayers, *Applied optics* **24**, 3359 (1985).
- [146] K. Kraus, A. Böhm, J. D. Dollard, and W. Wootters, *States, Effects, and Operations Fundamental Notions of Quantum Theory: Lectures in Mathematical Physics at the University of Texas at Austin* (Springer, 1983).
- [147] K. Nishida, Ambient seismic wave field, *Proceedings of the Japan Academy, Series B* **93**, 423 (2017).
- [148] S. L. Garrett, *Understanding acoustics: an experimentalist’s view of sound and vibration* (Springer Nature, 2020).
- [149] Y. Dain and R. M. Lueptow, Acoustic attenuation in three-component gas mixtures—theory, *The Journal of the Acoustical Society of America* **109**, 1955 (2001).
- [150] J. C. Owens, Optical refractive index of air: dependence on pressure, temperature and composition, *Applied optics* **6**, 51 (1967).
- [151] P. R. Saulson, Terrestrial gravitational noise on a gravitational wave antenna, *Physical Review D* **30**, 732 (1984).
- [152] S. Gruber and M. Marhic, Acoustic wave interaction with a coherent light beam, *The Journal of the Acoustical Society of America* **52**, 826 (1972).
- [153] S. M. Foreman, A. D. Ludlow, M. H. De Miranda, J. E. Stalnaker, S. A. Diddams, and J. Ye, Coherent optical phase transfer over a 32-km fiber with 1 s instability at 10-17, *Physical Review Letters* **99**, 153601 (2007).
- [154] A. V. Oppenheim, A. S. Willsky, and S. H. Nawab, *Signals & systems* (Pearson Educación, 1997).
- [155] K. Predehl, G. Grosche, S. Raupach, S. Droste, O. Terra, J. Alnis, T. Legero, T. Hänsch, T. Udem, R. Holzwarth, *et al.*, A 920-kilometer optical fiber link for frequency metrology at the 19th decimal place, *Science* **336**, 441 (2012).
- [156] N. R. Newbury, P. A. Williams, and W. C. Swann, Coherent transfer of an optical carrier over 251 km, *Optics letters* **32**, 3056 (2007).
- [157] S. P. Francis, T. T. Lam, K. McKenzie, A. J. Sutton, R. L. Ward, D. E. McClelland, and D. A. Shaddock, Weak-light phase tracking with a low cycle slip rate, *Optics Letters* **39**, 5251 (2014).
- [158] D. Matei, T. Legero, S. Häfner, C. Grebing, R. Weyrich, W. Zhang, L. Sonderhouse, J. Robinson, J. Ye, F. Riehle, *et al.*, 1.5  $\mu$  m lasers with sub-10 mhz linewidth, *Physical review letters* **118**, 263202 (2017).
- [159] R. W. Drever, J. L. Hall, F. V. Kowalski, J. Hough, G. Ford, A. Munley, and H. Ward, Laser phase and frequency stabilization using an optical resonator, *Applied Physics B* **31**, 97 (1983).
- [160] C. S. Sambridge, L. E. Roberts, A. R. Wade, J. T. Valiyakalayil, E. R. Rees, N. Chhabra, J. Zhang, A. J. Sutton, D. A. Shaddock, and K. McKenzie, Subfemtowatt laser phase tracking, *Physical Review Letters* **131**, 193804 (2023).
- [161] F. Salces Carcoba, A. Gupta, Y. Drori, R. Adhikari, L. Team, *et al.*, Optical frequency comb for cryogenic interferometer lock acquisition and calibration, in *APS April Meeting Abstracts*, Vol. 2022 (2022) pp. F01–069.
- [162] A. Gupta, F. Salces-Carcoba, Y. Drori, and R. Adhikari, 0.1% uncertainty multicolor calibration scheme for gravitational wave detectors, in *APS April Meeting Abstracts*, Vol. 2022 (2022) pp. F01–070.
- [163] M. Chwalla, K. Danzmann, M. D. Álvarez, J. E. Delgado, G. Fernández Barranco, E. Fitzsimons, O. Gerberding, G. Heinzel, C. Killow, M. Lieser, *et al.*, Optical suppression of tilt-to-length coupling in the lisa long-arm interferometer, *Physical Review Applied* **14**, 014030 (2020).
- [164] C. Cahillane, *Controlling and calibrating interferomet-*

- ric gravitational wave detectors* (California Institute of Technology, 2021).
- [165] K. Izumi, K. Arai, B. Barr, J. Betzwieser, A. Brooks, K. Dahl, S. Doravari, J. C. Driggers, W. Z. Korth, H. Miao, *et al.*, Multicolor cavity metrology, *Journal of the Optical Society of America A* **29**, 2092 (2012).
- [166] A. Staley, D. Martynov, R. Abbott, R. Adhikari, K. Arai, S. Ballmer, L. Barsotti, A. Brooks, R. DeRosa, S. Dwyer, *et al.*, Achieving resonance in the advanced ligo gravitational-wave interferometer, *Classical and Quantum Gravity* **31**, 245010 (2014).
- [167] P. M. Leung and T. C. Ralph, Quantum memory scheme based on optical fibers and cavities, *Physical Review A* **74**, 022311 (2006).
- [168] T. Pittman and J. Franson, Cyclical quantum memory for photonic qubits, *Physical Review A* **66**, 062302 (2002).
- [169] F. B. Früngel, *Optical Pulses-Lasers-Measuring Techniques* (Academic Press, 2014).
- [170] Edmund Optics, Laser Line Polarizing Plate Beamsplitters (2025), product No. 39878; accessed July 3, 2025.
- [171] S. Feng and H. G. Winful, Physical origin of the gouy phase shift, *Optics letters* **26**, 485 (2001).
- [172] O. Svelto, D. C. Hanna, *et al.*, *Principles of lasers*, Vol. 1 (Springer, 2010).
- [173] Z. Chai, X. Hu, F. Wang, X. Niu, J. Xie, and Q. Gong, Ultrafast all-optical switching, *Advanced Optical Materials* **5**, 1600665 (2017).
- [174] M. Schioppo, J. Kronjaeger, A. Silva, R. Ilieva, J. Patterson, C. Baynham, W. Bowden, I. Hill, R. Hobson, A. Vianello, *et al.*, Comparing ultrastable lasers at  $7 \times 10^{-17}$  fractional frequency instability through a 2220 km optical fibre network, *Nature communications* **13**, 212 (2022).
- [175] S. Droste, F. Ozimek, T. Udem, K. Predehl, T. Hänsch, H. Schnatz, G. Grosche, and R. Holzwarth, Optical-frequency transfer over a single-span 1840 km fiber link, *Physical review letters* **111**, 110801 (2013).
- [176] B. P. Dix-Matthews, S. W. Schediwy, D. R. Gozzard, E. Savalle, F.-X. Esnault, T. Lévêque, C. Gravestock, D. D’Mello, S. Karpathakis, M. Tobar, *et al.*, Point-to-point stabilized optical frequency transfer with active optics, *Nature communications* **12**, 515 (2021).
- [177] N. Hoghooghi, M. Mazur, N. Fontaine, Y. Liu, D. Lee, C. McLemore, T. Nakamura, T. Hayashi, G. Di Sciullo, D. Shaji, *et al.*, Enabling a multifunctional telecommunications fiber optic network: Ultrastable optical frequency transfer and attosecond timing in deployed multicore fiber, arXiv preprint arXiv:2410.13801 (2024).
- [178] S. Bregni and L. Primerano, Using the modified allan variance for accurate estimation of the hurst parameter of long-range dependent traffic, arXiv preprint cs/0510006 (2005).
- [179] N. Chandran, V. Goyal, R. Moriarty, and R. Ostrovsky, Position based cryptography, in *Annual International Cryptology Conference* (Springer, 2009) pp. 391–407.
- [180] S. Beigi and R. König, Simplified instantaneous non-local quantum computation with applications to position-based cryptography, *New Journal of Physics* **13**, 093036 (2011).
- [181] V. Asadi, R. Cleve, E. Culf, and A. May, Linear gate bounds against natural functions for position-verification, *Quantum* **9**, 1604 (2025).
- [182] J. Memmen, J. Eisert, and N. Walk, Advantage of multi-partite entanglement for quantum cryptography over long and short ranged networks, arXiv preprint arXiv:2312.13376 (2023).
- [183] R. Cleve, D. Gottesman, and H.-K. Lo, How to share a quantum secret, *Physical review letters* **83**, 648 (1999).
- [184] M. Hillery, V. Bužek, and A. Berthiaume, Quantum secret sharing, *Physical Review A* **59**, 1829 (1999).
- [185] M. Hein, W. Dür, J. Eisert, R. Raussendorf, M. Van den Nest, and H.-J. Briegel, Entanglement in graph states and its applications, in *Quantum computers, algorithms and chaos* (IOS Press, 2006) pp. 115–218.
- [186] D. Markham and B. C. Sanders, Graph states for quantum secret sharing, *Physical Review A* **78**, 042309 (2008).
- [187] A. Einstein *et al.*, Zur elektrodynamik bewegter körper, *Annalen der physik* **17**, 891 (1905).
- [188] J. P. Covey, I. Pikovski, and J. Borregaard, Probing curved spacetime with a distributed atomic processor clock, *PRX Quantum* **6**, 030310 (2025).
- [189] P. Wcisło, P. Ablewski, K. Beloy, S. Bilicki, M. Bober, R. Brown, R. Fasano, R. Ciuryło, H. Hachisu, T. Ido, *et al.*, New bounds on dark matter coupling from a global network of optical atomic clocks, *Science Advances* **4**, eaau4869 (2018).
- [190] T. Takano, M. Takamoto, I. Ushijima, N. Ohmae, T. Akatsuka, A. Yamaguchi, Y. Kuroishi, H. Mune Kane, B. Miyahara, and H. Katori, Geopotential measurements with synchronously linked optical lattice clocks, *Nature Photonics* **10**, 662 (2016).
- [191] G. Sagnac, Sur la preuve de la réalité de l’éther lumineux par l’expérience de l’interférographe tournant, *CR Acad. Sci.* **157**, 1410 (1913).
- [192] H. Thirring, Über die wirkung rotierender ferner massen in der einsteinschen gravitationstheorie., *Physikalische Zeitschrift* **19**, 33 (1918).
- [193] A. Lyons, G. C. Knee, E. Bolduc, T. Roger, J. Leach, E. M. Gauger, and D. Faccio, Attosecond-resolution hong-ou-mandel interferometry, *Science advances* **4**, eaap9416 (2018).
- [194] L. Arissian and J.-C. Diels, Intracavity phase interferometry: frequency combs sensor inside a laser cavity, *Laser & Photonics Reviews* **8**, 799 (2014).
- [195] M. O. Scully, M. S. Zubairy, and M. Haugan, Proposed optical test of metric gravitation theories, *Physical Review A* **24**, 2009 (1981).
- [196] X. Zhu, M. Lenzner, and J.-C. Diels, Phase nanoscopy with correlated frequency combs, *Sensors* **23**, 301 (2022).
- [197] J.-C. M. Diels, X. Zhu, and M. Lenzner, Sub-nano-scale phase sensing and improvement by squeezing, in *Quantum Sensing, Imaging, and Precision Metrology* (SPIE, 2023) p. PC1244710.
- [198] D. Fuentealba, J. Dahn, J. Steck, and E. Behrman, Robust and scalable quantum repeaters using machine learning, Preprints 10.20944/preprints202505.0691.v1 (2025).
- [199] V. Giovannetti, S. Lloyd, and L. Maccone, Quantum random access memory, *Physical review letters* **100**, 160501 (2008).
- [200] G. Brassard, H. Buhrman, N. Linden, A. A. Méthot, A. Tapp, and F. Unger, Limit on nonlocality in any world in which communication complexity is not trivial, *Physical Review Letters* **96**, 250401 (2006).

- [201] S. Popescu and D. Rohrlich, Quantum nonlocality as an axiom, *Foundations of Physics* **24**, 379 (1994).  
 [202] B. S. Cirel'son, Quantum generalizations of bell's inequality, *Letters in Mathematical Physics* **4**, 93 (1980).  
 [203] D. Ding and L. Jiang, Coordinating decisions via quantum telepathy, arXiv preprint arXiv:2407.21723 (2024).

## Appendix A: Reflection Device

When the physical separation of the VBG connected termination stations is greater than 100 km, it is necessary to deploy mirrors to deflect the beam to overcome the curvature of the Earth, which is a problem that has been previously addressed in a satellite-based scheme [6]. For a realistic depth  $D$  for deploying the VBG channel, the maximum separation between two mirror stations can be estimated as

$$L_{\text{mirror}} \approx \sqrt{8R_E D}, \quad (\text{A1})$$

where  $R_E \approx 6370\text{km}$  is the radius of the Earth. If we plug in a reasonable depth  $D \approx 30\text{m}$  given by the common selection to build a subway, we get  $L_{\text{mirror}} \leq 40\text{ km}$ , which means that we need to deploy 1 mirror every 10 sections, assuming  $L_0 = 4\text{ km}$ . However, it can definitely be further pushed to 100 km, allowing for a depth of approximately 200m by carefully selecting the location using the fluctuation of the Earth's radius. Alternatively, with a significantly higher cost, this number only increases with the square root of depth. As a result, the ratio of the effective additional attenuation introduced by the mirrors to the default attenuation is calculated as

$$A \equiv \frac{\alpha_{\text{mirror}}}{\alpha_{\text{default}}} \approx \frac{L_0}{L_{\text{mirror}}} \times \frac{l_{\text{mirror}}}{l_{\text{default}}} \approx \frac{l_{\text{mirror}}}{10l_{\text{default}}}, \quad (\text{A2})$$

where  $\alpha_{\text{default}}$  and  $l_{\text{default}}$  are the attenuation factor and section loss, respectively, assuming the all-lens configuration. We will require the factor to be smaller than one in order to maintain the performance of VBG. Thus, the loss introduced by the mirror shall not be more than one order of magnitude worse than the minimum default total loss, that is,  $\sim 300\text{ppm}$ .

This loss can be estimated following almost the same recipe as the lens, which gives a similar requirement for the radius, coating, and translational alignment. However, the loss introduced by the angular misalignment, which is negligible in the lens case, may now become a serious problem and dominate the additional loss introduced by the mirror. We shall estimate this loss using the mode-expansion approach in this section, with two different reflection device designs.

### 1. Single 45° Incident Mirror

For the simplest model, we consider using a single-plane mirror with an incident angle of  $\frac{\pi}{4}$  to deflect the

beam, as shown in Fig. 7 (a), and decompose the rotation into two independent DOFs, namely tipping  $\delta\beta_s$  and tilting  $\delta\beta_p$  with respect to the center point of the mirror. For the loss introduced by the tip, one can show by a simple argument on the solution of the Helmholtz equation and by rotating the optical axis for the plane mirror that the loss and phase shift depend only on the misalignment angle, regardless of its original orientation angle  $\beta_s$  [116]. This allows us to consider only the case  $\beta_s = 0$ , while the effects of tilt angle misalignment  $\delta\beta_p$  can be converted into an effective tipping angle of  $\delta\beta_s^{\text{eff}} \approx \frac{\sqrt{2}}{2}\delta\beta_p$ .

Suppose that the mirror is located at location  $z$  with respect to the beam waist, then the additional phase gain at the plane can be expressed as

$$\exp(ik 2\delta\beta r \cos \phi) \approx 1 + i\delta\beta_s k r (e^{i\phi} + e^{-i\phi}), \quad (\text{A3})$$

which results in a conversion factor into  $E_0^1$  and  $E_0^{-1}$  Laguerre-Gaussian modes with a factor

$$M_{00 \rightarrow (0, \pm 1)} \approx i \frac{w(z)}{\sqrt{2}} k \delta\beta_s. \quad (\text{A4})$$

with  $w(z)$  being the spot size at location  $z$ . One notices that there is no direct first order coupling into phase noise, while the loss is given by

$$l_{\delta\beta_s} \approx k^2 w^2(z) \delta\beta_s^2 \sim \left( \frac{\delta\beta_s}{\beta_G} \right)^2, \quad (\text{A5})$$

where  $\beta_G = \frac{\lambda}{\pi w(0)} \sim 10^{-5}\text{rad}$  is the divergence angle of the Gaussian beam, and this agrees well with the reference [117]. One also finds that the loss is minimized when the mirror is placed at the waist. Then, we have

$$l_{\delta\beta_s} \approx \frac{2\pi L_0}{\lambda} F \delta\beta^2, \quad (\text{A6})$$

where  $F = \sqrt{\frac{4f}{L_0} - 1} \approx 1$  for a confocal configuration. For an order of degree estimation, plugging in  $\delta\beta_s \approx 0.1\mu\text{rad} \sim 1\% \beta_G$ , one finds that  $l_{\delta\beta_s} \approx 160\text{ppm}$  for the default configuration, which is also the level of alignment precision required to maintain the performance of VBG.

Attaining the required alignment level is challenging, yet feasible with current technology. The most analogous setup to ours involves the alignment of the input beam in LIGO, where the control system operates at normal pressure rather than under vacuum [118]. Two piezo-tip/tilt actuators and two quadrant photon detectors are used to handle the alignment. The sensing system achieves sub-nanoradian precision, detecting high-frequency noise, with angular movement post-correction below  $0.01\mu\text{rad}$  rms. Notably, in an ultrahigh vacuum, the test masses achieved an rms of  $3\text{nrad}$  [119], surpassing our requirements by two orders of magnitude. Compared to the satellite system, the satellite system has shown a dynamic tracking error of less than  $0.4\mu\text{rad}$  [7], despite operating in a noisier environment.

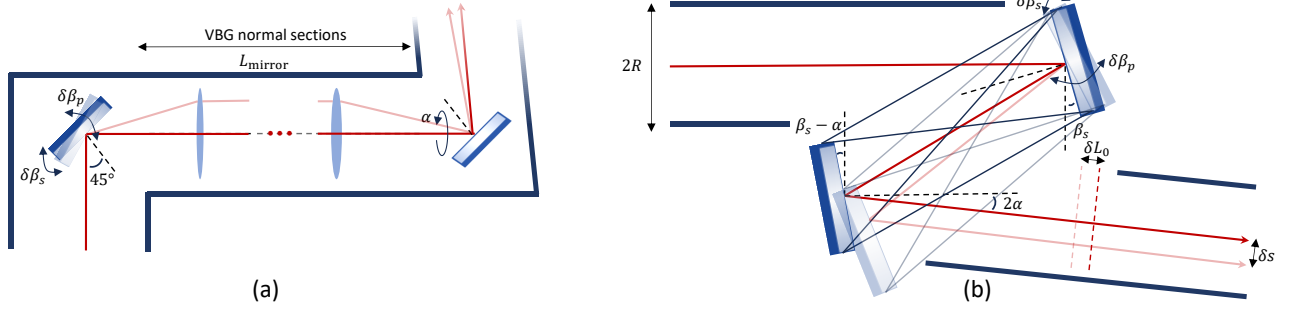


FIG. 7. The illustration of two reflector models. (a) The single  $45^\circ$  Incident mirror is used to first deflect the light by  $90^\circ$ , then the mirror in the next mirror section is rotated by  $\alpha$  with respect to the optical axis of the system to deflect the light to overcome the curvature. (b) The retro-reflector consisting of two mirrors binding together as a rigid body with a separation angle of  $\alpha$  is used to deflect the light beam by  $2\alpha$ . The transparent mirrors and light beam represent the configuration after a rotation perturbation of  $\delta\beta_s$  with respect to the center point of the first mirror and the rotation axis perpendicular to the incident plane.

## 2. Two-Mirror Rigid Retro-Reflector

A slightly more complicated mirror system, as shown in (b) utilizing the tricks of the Moon retro-reflector [120–122] can further relieve the requirement, where the two mirrors are bound together by a rigid structure and are assumed to rotate as a whole with respect to the center point of the first mirror. And again, the rotation perturbation is decomposed into tipping  $\delta\beta_s$  and tilting  $\delta\beta_p$  with fixed tipping angles  $\beta_s$  and  $\beta_s - \alpha$ , respectively, to carry the beam deflection to an angle of  $2\alpha$ .

Through simple but heavily labored geometric analysis, one finds that upon perturbation, to the first order, one results in effective transverse and parallel displacement perturbations of the beam as

$$\begin{aligned} \delta\beta_s &\rightarrow (\delta L_0, \delta s)_s = 2d\delta\beta_s(\cos^2(\beta_s + \alpha), \sin[2(\beta_s + \alpha)]), \\ \delta\beta_p &\rightarrow (\delta L_0, \delta s)_p = 2d\delta\beta_p(0, \cos\beta_s), \end{aligned} \quad (\text{A7})$$

after which, one can apply the developed misalignment formula to calculate the loss [10]. A key observation is that the parallel displacement loss is negligible compared to the transverse one, as it will be suppressed by a factor of  $\frac{1}{L_0}$ . Their cross-term also vanishes because the mode conversion is different and orthogonal. To give an estimation of the magnitudes, the deflection angle  $\alpha$  and the separation  $d$  can be calculated as

$$\alpha \approx \frac{L_{\text{mirror}}}{2R_E} \sim 3 \times 10^{-3}, \quad d \geq \frac{2R_{\text{mirror}}}{\sin\theta}, \quad (\text{A8})$$

where  $R_{\text{mirror}} \approx 12\text{cm}$  is the radius of the mirror, and the latter condition arises from the requirement that the mirrors do not block each other. As an example calculation, suppose  $\beta_s = 10^\circ$  is required for the maintenance of polarization. Then we have

$$\delta s \approx \frac{\delta\beta_{s/p}}{0.1\text{rad}}(0.3\text{mm}), \quad \delta L_0 \approx \frac{\delta\beta_s}{0.1\text{rad}}(-50\mu\text{m}); \quad (\text{A9})$$

and one concludes that the requirement for angle alignment precision is loosened by three orders of magnitude.

This scheme has several advantages: the incident plane is not required to rotate for deflection, which helps avoid the static birefringence effects discussed in Sect. B 4; the effective refractive index can be made close to 1 instead of being lower-bounded by  $\sqrt{2}$  since the light propagates in almost a straight line; all first order translation perturbation effects are suppressed by a factor of  $\alpha \sim 10^{-3}$ , which also relaxes the requirement by three orders of magnitude. However, there is no free lunch, as the angle perturbation is now directly coupled to the phase noise via  $\delta L_0$ .

## Appendix B: Details of Noise Budgets

In this section, we provide a detailed description of noise budgets for estimating the phase noise power spectral density, as summarized in Fig. 8, following a comparative and extrapolative method using the data and analysis from advanced LIGO [21–23].

### 1. Seismic and Alignment Noise

The seismic waves of the Earth will introduce movement into the system and cause phase noise. Empirically, the phase noise is dominated by  $k\delta z$ , with  $\delta z$  representing the parallel movement. We will present a theoretical derivation based on the Laguerre-Gaussian mode expansion that we have used to derive the loss for cross-verification. Then, we provide a simple suspension design for the optical isolation platform and estimate both its translation and rotation induced noise power spectrum based on the measured and theoretical seismic movement.

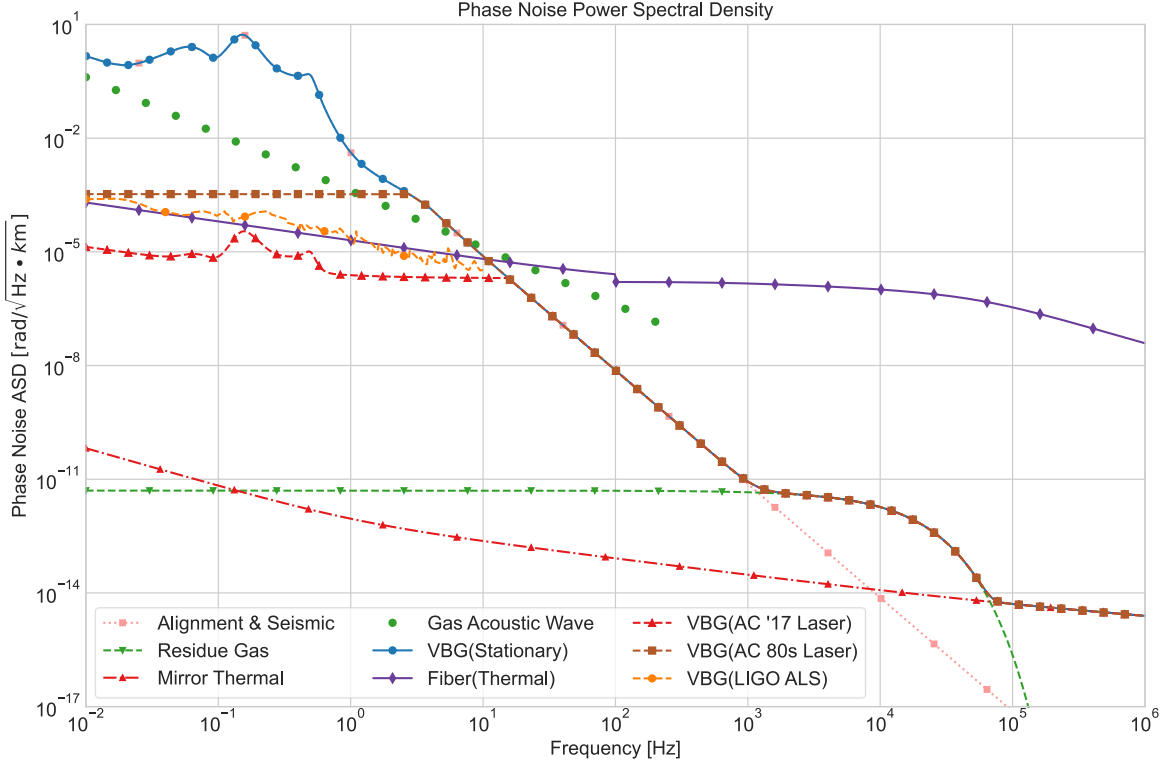


FIG. 8. Normalized phase noise amplitude spectral density of the VBG before and after section-wise active noise cancellation with different techniques in comparison with fiber thermal noise [41–43] and the detailed noise budget. The nonstationary acoustic wave excitation, assuming a 20dB level (measured in 1 atm), is also shown separately as green scatters. The contributions from reflector sections will at most increase the noise by 10% and thus are not shown here.

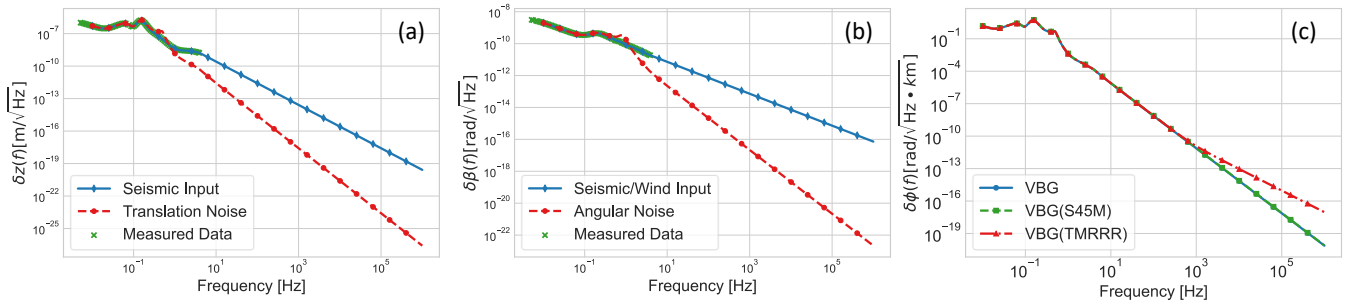


FIG. 9. The noise ASD of the seismic/wind input, passive isolated platform and their contributions to the final PNASD. (a) Translation movement ASD. (b) Rotation movement ASD. (c) The expected contribution to PNASD.

### a. Lens Section

**Parallel Movement.** To estimate the noise induced by parallel movement, we set the location of the lens to  $\frac{L_0}{2} + \delta z$  and expand the fundamental field to the first order of  $\delta z$ , collecting the imaginary term in the coefficient of the fundamental field. After which, one finds that, to the first order, the phase is given by

$$\delta\phi = i \left( -k + \frac{1 - F^2}{F} \frac{1}{L_0} + \frac{2F}{F^2 + 1} \frac{1}{L_0} \right) \delta z, \quad (\text{B1})$$

with the second and third terms in the parentheses coming from the curvature term and the Gouy phase, respectively, which are greatly suppressed by the section length  $L_0$  and thus negligible compared to  $k\delta z$ .

**Transversal Displacement.** Similarly, let  $\delta s$  denote the offset of the beam. Then, we obtain a transform of the lens coordinate  $r$  into the beam parameter  $r'$  as

$$r \rightarrow \sqrt{r^2 + \delta s^2 - 2r\delta s \cos\theta}, \quad (\text{B2})$$

with  $\theta$  being the angular coordinate. One notices that the perturbation  $\delta s$  can only couple to the phase in the

second order via

$$\delta\phi = -i \frac{1}{1+F^2} \frac{k\delta s^2}{L_0}, \quad (\text{B3})$$

which is negligible due to the suppression factor  $\frac{\delta s}{L_0}$  compared to parallel displacement.

**Rotation.** One can expect that the phase shift is of second order in  $\delta\beta_{s/p}$ . And following a simple geometric statement, one estimates it to be

$$\delta\phi \approx \frac{kd}{2n^2} \delta\beta_{s/p}^2, \quad (\text{B4})$$

with  $d$  being the thickness of the lens and  $n$  being the effective refractive index of the lens. The coupling is also found to be negligible compared to  $k\delta z$  under the default configuration.

#### b. Reflector Section

The contribution from the reflector section will be suppressed by  $\sqrt{\frac{L_0}{L_{\text{mirror}}}} \sim 1/3$  compared to the lens section.

**Translation Movement.** One can directly apply the results from the lens to calculate the coupling of translational movement into phase noise, noting that the effects associated with parallel and transverse displacement do not couple in the leading order, even if their perturbations are coupled.

For the S45M configuration, the translation movement is decomposed into the movement parallel to the mirror,  $\delta s_{\parallel}$ , and  $\delta s_{\perp}$ , which is orthogonal to the mirror. And one directly finds that  $\delta s_{\perp}$  gives rise to an effective parallel displacement  $\delta z_{\text{eff}} = \frac{\sqrt{2}}{2} \delta s_{\perp}$ , while  $\delta s_{\parallel}$  has a trivial contribution according to the analysis of the lens.

As for the TMRRR configuration, we have shown in Appendix A 2 that the contribution is suppressed by the deflection angle  $\alpha \sim 10^{-3}$  and is thus negligible.

**Rotation.** The effects of rotation have also been calculated in Sec. A.

For the S45M configuration, it is clear from Eq. A3 that there is no first-order coupling, and the coupling is at least third order, which makes it negligible.

While the TMRR configuration, rotation couples to the phase noise via  $\delta L_0$  and can be calculated as

$$\delta\phi \approx -4kR_{\text{mirror}} \cos(\beta_s) \delta\beta_s, \quad (\text{B5})$$

where we have dropped the small deflection angle  $\alpha$ , and there is no contribution from  $\delta\beta_p$ .

#### c. Seismic Input

Generally, seismic-induced **translation** rolls off as  $\delta z(f) \sim \frac{1}{f^2}$  while establishing several peaks and long-term drift at low frequency [40, 123]. Therefore, to estimate the seismic-induced translation movement, we can

use the measured data from the LIGO sites and extrapolate the spectrum to high frequencies, assuming the aforementioned  $\frac{1}{f^2}$  scaling, the data of which is shown in Fig. 9 (a).

As for the **rotation**, the low-frequency part is dominated by the wind, and we can also use the measured data from LIGO during the low wind operation[124] for an upper bound. The stationary high-frequency part is mainly attributed to the seismic movement. By assuming a seismic wave propagating with displacement  $z(x, t)$ , we can calculate the induced tilting as

$$\delta\beta(x, t) = \frac{\partial z(x, t)}{\partial x} \approx kz. \quad (\text{B6})$$

Therefore, the PSD of the tilting can be calculated from the PSD of the seismic-induced translation as

$$S_{\beta}(f) \approx k^2 S_z(f) \approx \left(\frac{2\pi f}{c_s}\right)^2 S_z(f), \quad (\text{B7})$$

where  $c_s$  is the speed of the seismic wave and can be considered roughly a constant for a given depth [125]. We estimate the wave speed to be 2.2km/s by fitting the measurement tilting data with the measured translation data at relatively high frequency, which agrees with the typical seismic surface wave speed [126]. The tilting input data for the following calculation, obtained from both measurement and the above theoretical model, is plotted in Fig. 9 (b).

#### d. Passive Isolation Platform

We assume a simple scheme that utilizes two springs for the suspension of each degree of freedom (DOF). In this setup, the optical table acts as a rigid body, isolated by pairs of parallel springs, as shown in Fig. 10 (a), from which the transmissibility can be expressed as [127, 128]

$$T_z(f) = \sqrt{\frac{1 + \left(2\xi \frac{f}{f_n}\right)^2}{\left(1 - \left(\frac{f}{f_n}\right)^2\right)^2 + \left(2\xi \frac{f}{f_n}\right)^2}}, \quad (\text{B8})$$

where  $\xi \approx 0.1$  and  $f_n \approx 0.5\text{Hz}$  are the typical damping ratios and natural (resonant) frequencies for a commercial passive isolated optical table, respectively.

The transmissibility for the angular rotation movement can be calculated using a similar method by substituting the mass with the moment of inertia and the force with the torque, which leads to essentially the same expression, [129, 130]

$$T_{\beta}(f) = \sqrt{\frac{1 + \left(2\xi_{\beta} \frac{f}{f_{n,\beta}}\right)^2}{\left(1 - \left(\frac{f}{f_{n,\beta}}\right)^2\right)^2 + \left(2\xi_{\beta} \frac{f}{f_{n,\beta}}\right)^2}}, \quad (\text{B9})$$

with  $\xi_\beta = \sqrt{3}\xi$ ,  $f_{r,\beta} = \sqrt{3}f_r$  being the natural frequency and damping ratio for the rotation, respectively. The estimated transmissibility curve of the passive isolation is plotted in Fig. 10 (b) in comparison to the measured data of the commercially available one, which matches well with our prediction.

Therefore, the final platform performance is determined by the product of the raw input movement and the transmissibility, with the translation and rotation movement ASD, as well as the expected contribution to the total phase noise, being shown in Fig. 9. It shall be remarked here that, although we do not explicitly include the active feedback scheme to stabilize the platform, which is performed before the suspension in LIGO [39, 131], we still need those inertial or relative sensors and servos to perform global alignment calibration to remove low-frequency drifts or flicker noises, whose typical integration diverges as  $\sim \ln(1/f_l)$  with  $f_l$  going to zero due to the non-stationary property [132, 133]. This can be accomplished using the alignment methods mentioned in the loss estimation section or by performing differential measurements that reject the common noise. As the performance PSD is estimated from 0.2Hz in this work, we expect a global calibration process to be conducted for every  $T_{cal} \sim 100$ , which shall be feasible given that the maximum signal delay allowed in VBG is no more than 1. Increasing the calibration period when needed,  $T_{cal}$ , is also possible and will not significantly change the rms noise due to the logarithmic scaling.

## 2. Residue Gas Noise

As the default residue gas pressure in VBG is 1 Pascal, which is approximately seven orders of magnitude higher than that of LIGO, residue gas effects can result in significant phase noise and require careful estimation. In addition, such a residual gas pressure level will allow a broad band of the acoustic wave to propagate within the tube since it exceeds the cut-off gas pressure, which does not need to be considered in LIGO. However, we will leave the detailed discussion on this topic to be included in the Appendix B 5, as there are many effective approaches to avoid it, in addition to reducing residual gas pressure. Unlike LIGO, the damping effect of the residual gas will be dominated by the seismic movement and suppressed by the suspension, and thus omitted here [135]. Therefore, in this section, we will discuss the scattering caused by residual gas, which is also investigated in LIGO.

The interaction between the gas residue molecules and the light under thermal equilibrium will also introduce scattering phase noise, which is dominated by the forward scattering and can be estimated by [136]

$$\delta\phi = \frac{(2\pi)^2 \alpha \sqrt{\rho_\# L_0}}{\lambda \sqrt{w_0 v_0}} e^{-\sqrt{2\pi} \frac{w_0}{v_0}}, \quad (\text{B10})$$

where  $\alpha$  is the molecular polarizability,  $\rho_\#$  is the particle

number density,  $v_0$  is the thermal velocity of the gas, and  $w_0$  is the average radius of the beam. And for our configuration, again, assuming  $N_2$  is dominating, we have

$$\delta\phi \approx 10^{-11} \times \left( \frac{1550\text{nm}}{\lambda} \right)^{\frac{5}{4}} \sqrt{\frac{P}{1\text{Pa}}} e^{-\frac{f}{10\text{kHz}}} \text{rad}/\sqrt{\text{Hz}}. \quad (\text{B11})$$

## 3. Thermal Noise

The thermal noise mainly consists of suspension thermal noise and mirror thermal noise, while the former is washed away by seismic, alignment, and control noise, as the mirrors are not directly hung on a relatively rigid body but instead on a fiber quad-pendulum. As for the mirror noise, it may include Brownian noise, thermo-optic noise, and thermal-elastic noise for both the substrate and the coating.

Assuming that we use the same materials for the substrate and coating as LIGO, the thermal noise for the mirror will be dominated by the coating Brownian noise, which can be calculated using the fluctuation-dissipation theorem as [137]

$$\delta\phi = \frac{2\pi}{\lambda} \sqrt{\frac{2k_B T d_c}{\pi^2 f w^2 Y} \left( \frac{Y'}{Y} \phi_{\parallel} + \frac{Y}{Y'} \phi_{\perp} \right)}, \quad (\text{B12})$$

where  $w$  is the beam radius at the mirror,  $\phi_{\parallel}$  and  $\phi_{\perp}$  are the parallel and orthogonal loss angles of the coating, respectively,  $Y$  and  $Y'$  are the Young's moduli for the substrate and the coating,  $d_c$  is the thickness of the coating. Using the values from LIGO, one gets that [138]

$$\delta\phi_{BN,c} = 8.84 \times 10^{-13} \left( \frac{1550\text{nm}}{\lambda} \right)^{3/2} \left( \frac{1\text{Hz}}{f} \right)^{0.45} \text{rad}/\sqrt{\text{Hz}}, \quad (\text{B13})$$

where the deviation from  $-0.5$  scaling may arise from the frequency dependence of the loss angle.

However, as the lenses constitute the major optics in our VBG design and the thermal noise budgets for transmissive optics are different from the reflective ones, we shall re-estimate the contributions from all the aforementioned mechanisms.

For the Brownian noise, if we assume the same materials are used for the AR coating as well as the substrate, then the Brownian noise will essentially be at the same level, as the mechanism depends on whether the light passes through it or is reflected (in fact, it will be slightly smaller) [139]. Therefore, we can re-use Eq. (B13) for the estimation of Brownian noise for lenses.

As for thermal noise, the HR coating for the mirrors used in LIGO is designed and optimized specifically to make the thermal-elastic and thermal refractive noise cancel coherently, resulting in an order of magnitude suppression of total thermal noise [140]. For our AR coating estimation, we can simply treat them incoherently to provide a conservative estimate.

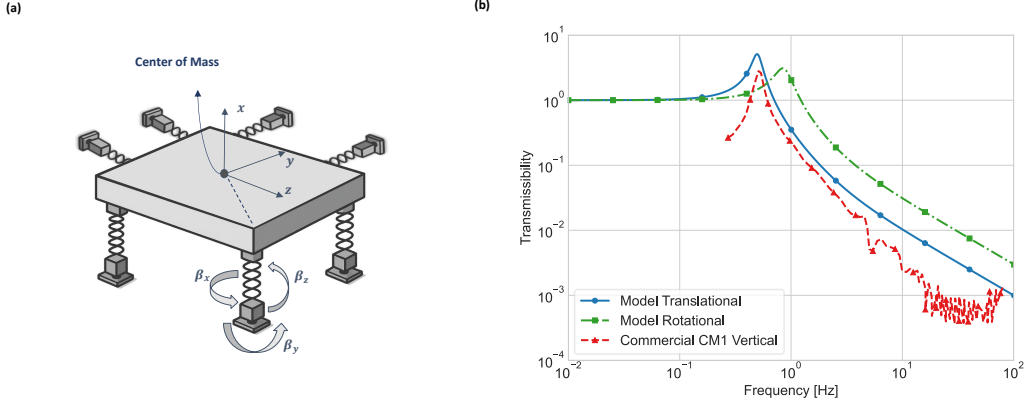


FIG. 10. The (a) illustration and the (b) performance of the passive suspension system. The vertical transmissibility performance of the commercially available CM1 optical table [134] is also plotted for comparison.

The thermal noise in coatings is directly related to the thermal fluctuations given as

$$S_T = \frac{2\sqrt{2}}{\pi} \frac{k_B T}{w^2 \sqrt{\kappa C \omega}}, \quad (\text{B14})$$

where  $w$  is the beam radius,  $\kappa$  is the thermal conductivity, and  $C$  is the heat capacity per volume. For the thermal elastic noise, it can be calculated from Eq. (B14) as

$$S_z^{TE} = \left( \bar{\alpha}_c d_c - \bar{\alpha}_s \frac{C_c}{C_s} d_c \right) S_T, \quad (\text{B15})$$

where  $\bar{\alpha}$  is the effective thermal expansion coefficient, with subscripts indicating substrate or coating, and  $d_c$  is the thickness of the coating. And for the thermal refractive noise, the displacement noise can be derived as

$$S_x^{TR} = (\bar{\beta} \lambda)^2 S_T, \quad (\text{B16})$$

where  $\bar{\beta}$  is the effective refractive index response to the temperature. Using the data from LIGO, the noise power spectrum for the lens coating is estimated to be (as the HR coating ( $\sim 9\mu\text{m}$ ) used in LIGO is thicker than our AR coating design ( $\sim 1\mu\text{m}$ ), a rescaling of the data from LIGO serves as an upper bound [140, 141]):

$$\delta\phi_{TE,c}(f) \approx 7.3 \times 10^{-14} \left( \frac{1550\text{nm}}{\lambda} \right)^{\frac{3}{2}} \left( \frac{1\text{Hz}}{f} \right)^{\frac{1}{4}} \text{ rad}/\sqrt{\text{Hz}} \quad (\text{B17})$$

$$\delta\phi_{TR,c}(f) \approx 3.5 \times 10^{-14} \left( \frac{1550\text{nm}}{\lambda} \right)^{\frac{3}{2}} \left( \frac{1\text{Hz}}{f} \right)^{\frac{1}{4}} \text{ rad}/\sqrt{\text{Hz}} \quad (\text{B18})$$

While for the lens' substrate, the bulk transmission thermal-optic noise can be calculated as [142, 143]

$$S_x^{TO}(f) = \frac{16k_B \kappa T^2 \beta_{eff}^2 d}{\pi C^2 \rho^2 w^4 \omega^2}, \quad (\text{B19})$$

where  $\beta_{eff} = \frac{dn}{dT} + \alpha(n-1)$  is the effective thermal response,  $d \sim 2\text{cm}$  is the thickness of the substrate, and other parameters are defined as before but for the substrate. Then, the thermal-optic noise for the substrate can be numerically estimated as

$$\delta\phi_{TO,s}(f) \approx 1.3 \times 10^{-12} \left( \frac{1\text{Hz}}{f} \right) \left( \frac{1550\text{nm}}{\lambda} \right)^2 \quad (\text{B20})$$

The thermal noise budget for the lens, including all the relevant components, is shown in Fig. 11. From this, we observe that the substrate thermal-optic noise dominates at low frequency, while the coating Brownian noise dominates at high frequency, as is the case with the mirror.

#### 4. Birefringence Noise

The birefringence effects of the substrate and the coating will not only disrupt the polarization stability but can also couple to the phase noise if the orientation of the optic axis of each optical component is perturbed relative to the polarization of the signal light. The analysis from LIGO recently addresses this issue in a coherent way [44] since it has a cavity with light bouncing back and forth. We will follow a similar treatment while taking into account the incoherent nature of perturbation in the VBG system. The light transmitted in the VBG system can be decomposed into parallel and orthogonal polarization with respect to the selected axis (e.g. the crystal axis of the first input lens), described using the Jones matrix as below

$$\vec{E} = \begin{bmatrix} E_{\parallel} \\ E_{\perp} \end{bmatrix}. \quad (\text{B21})$$

Then, when the ordinary axis of the mirror/lens (including the coating) is aligned with  $E_{\parallel}$ , the transfer matrix

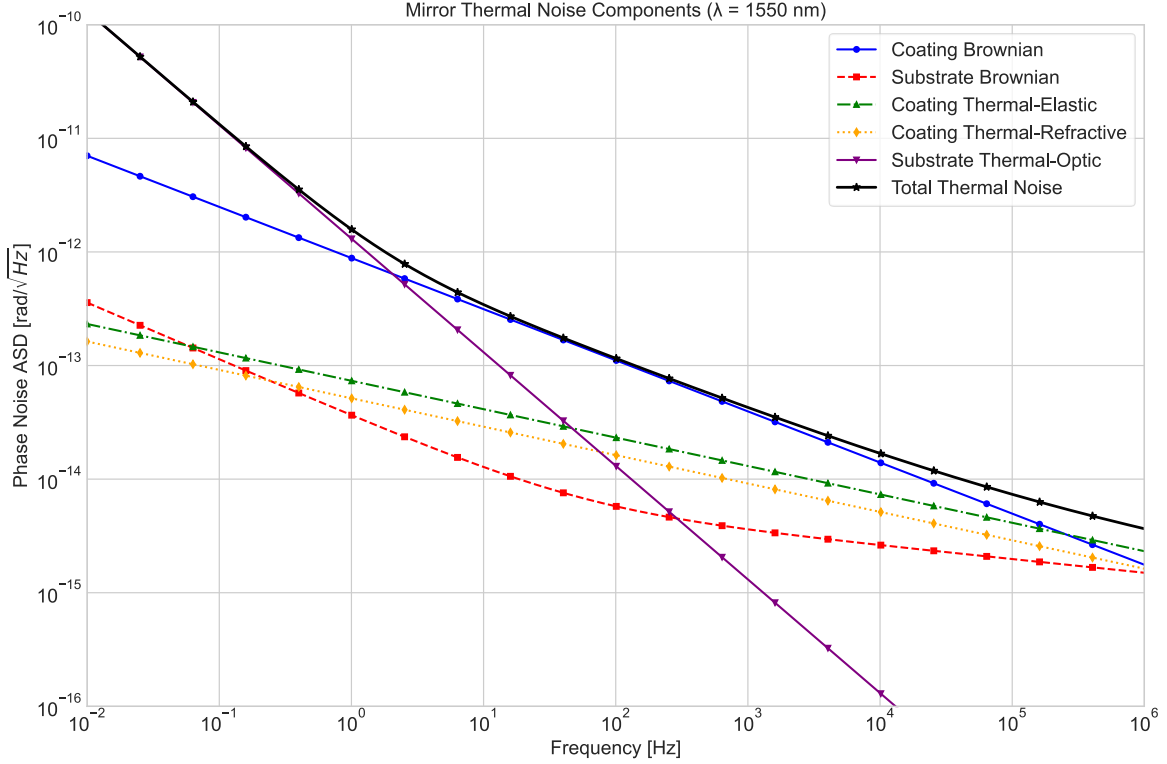


FIG. 11. Thermal noise budget for the lenses at the center carrier wavelength  $\lambda = 1550\text{nm}$ .

can be represented as

$$T_{m/l} = t_0 \begin{pmatrix} 1 & 0 \\ 0 & (1-t)\exp(i\phi_{m/l}) \end{pmatrix}. \quad (\text{B22})$$

where  $t_0$  represents the overall transmission, with  $t$  being the difference between two orthogonal polarization modes, which must be smaller than 100ppm according to the loss requirement as well as the available mirror/lens coating. In addition,  $\phi_{m/l}$  is the birefringence phase shift. For a lens, it is dominated by the substrate phase shift calculated as

$$\phi_l = kd\delta n \sim 0.01\text{rad}, \quad (\text{B23})$$

with  $\delta n \sim 10^{-7}$  for silica substrate and  $d \sim 0.02\text{m}$  for the lens being used in VBG. While for the mirrors, it is determined by the birefringence of the coating and is found to be  $\phi_m \sim 10^{-4}\text{rad}$  for the  $\text{Ta}_2\text{O}_5/\text{SiO}_2$  coating that we plan to use [144, 145]. And when the axis of the mirror/lens is rotated by an angle  $-\theta$ , the transform matrix is

$$T_{m/l}(\theta) = T_{m/l}R(\theta), \text{ with } R(\theta) = \begin{pmatrix} \cos\theta & -\sin\theta \\ \sin\theta & \cos\theta \end{pmatrix}, \quad (\text{B24})$$

assuming we always select the crystal axis of the last optical component as the reference frame. Suppose there is a perturbation  $\delta\theta$ . Then, to the first order, one gets

that

$$\begin{aligned} T_{m/l}(\theta + \delta\theta) &= t_0 \begin{pmatrix} 1 & 0 \\ 0 & e^{i\phi_{m/l}} \end{pmatrix} R(\theta) \\ &\quad - t_0 \begin{pmatrix} 0 & 0 \\ 0 & e^{i\phi_{m/l}} \end{pmatrix} R(\theta)t \\ &\quad - t_0 \begin{pmatrix} 1 & 0 \\ 0 & e^{i\phi_{m/l}} \end{pmatrix} R(\theta)J\delta\theta, \end{aligned} \quad (\text{B25})$$

where  $J = \begin{pmatrix} 0 & 1 \\ -1 & 0 \end{pmatrix}$ . The static unperturbed transform can be corrected at the end by applying the inverse of the transform as

$$T^r = R^\dagger(\theta) \begin{pmatrix} 1 & 0 \\ 0 & e^{-i\phi_{m/l}} \end{pmatrix}. \quad (\text{B26})$$

When the constant shifting angle  $\theta = 0$  is considered, only the last term will cause a conversion into the other mode with a conversion factor  $t_0 e^{i\phi} \delta\theta$ . This means that if we simply discard the orthogonal polarization in this case, the loss will be of order  $\delta\theta^2 \sim 1\text{ppm}$  given  $\delta\theta_{rms} \sim 1\text{mrad}$  [45], which can be safely neglected, and the coupling between loss and the phase will be trivial even if we choose a poor encoding.  $\theta = 0$  will correspond to the lens section as well as the TMRRR reflector, while for the S45M section,  $\theta \approx \alpha \sim 1\text{mrad}$  may be inevitable.

Consider the case  $\theta = 0$  and assume that  $E_\perp = 0$ . In this case, if we set  $t = 1$  and completely destroy the polarization, there shall be no notable phase noise. If we

want to allow for polarization coding, there is a risk that the light from the orthogonal mode may converge back and interfere with the phase. However, since the conversion phase is stochastic due to the random misalignment  $\delta\theta$ , we can assume that the light in the orthogonal mode has no correlation with the light in the parallel mode, and thus the net effect is to lower the visibility in the fundamental mode. As long as the power in the orthogonal mode is not significant (passing through fewer than  $10^6$  sections), this effect can be safely neglected. As for the S45M section, it is expected that it shall not be used for polarization encoding, and the polarizer filter shall be applied. The additional loss due to projection will be proportional to  $\sin^2\theta$ , which is around 1ppm since  $\theta \sim \alpha \sim 10^{-3}\text{rad}$ .

However, for polarization encoding, birefringence can lead to phase noise between the two encoded states  $|0\rangle$  and  $|1\rangle$ . In addition, the difference in transmission rate,  $t$ , may also introduce amplitude noise. The naive solution for the latter may be to alternate the orientation of the optic axis of sequential lenses between  $0^\circ$  and  $90^\circ$ , which allows for the cancelation of the transmission difference and phase shift difference between the two polarized modes. However, the sequential misalignment angle  $\delta\theta$  is randomized and may still introduce phase noise and amplitude noise, which we shall estimate here. We assume the phase difference between two modes is  $\phi_0$ . Then, the input Jones matrix can now be written as

$$|\psi\rangle \sim \vec{E} = \begin{bmatrix} E_{\parallel} \\ E_{\perp} e^{i\phi_0} \end{bmatrix}. \quad (\text{B27})$$

Then, we can derive the transform matrix for two consecutive lenses/mirrors as

$$\begin{aligned} T_{1,m/l} \left( \frac{\pi}{2} + \delta\theta_2 \right) T_{2,m/l}(\delta\theta_1) &\approx t_0^2 \times \left\{ (1 - \bar{t})I \right. \\ &- \delta t_1 \begin{pmatrix} 0 & 0 \\ 0 & 1 \end{pmatrix} - \delta t_2 \begin{pmatrix} 1 & 0 \\ 0 & 0 \end{pmatrix} \\ &+ i(\delta\phi_1 - \delta\phi_2) \begin{pmatrix} 0 & 0 \\ 0 & 1 \end{pmatrix} \\ &\left. - \delta\theta_1 \begin{pmatrix} 0 & 1 \\ -1 & 0 \end{pmatrix} - \delta\theta_2 \begin{pmatrix} 0 & e^{i\bar{\phi}} \\ -e^{-i\bar{\phi}} & 0 \end{pmatrix} \right\}, \end{aligned} \quad (\text{B28})$$

where we set  $t_i = \bar{t} + \delta t_i$ ,  $\phi_{m/l,i} = \bar{\phi} + \delta\phi_i$  for each lens/mirror to separate the relatively small statistical differences of each lens/mirror. In addition, the second-order terms are not included, as it is a well-known fact that they only contribute to the trivial Kraus operators [146]. The second two terms can be decomposed into an overall attenuation and a dephasing channel, while the third term is just the well-known dephasing terms due to the inhomogeneous phase. The last two terms are directly related to the misalignment, which we expect to dominate: the first term represents a bit flip, while the second term represents the combined effects of bit flip and phase shift. While one can average the effects and arrive at the effective Kraus operators for each lens/mirror as

follows

$$\frac{\delta\theta}{\sqrt{2}} \left\{ \begin{pmatrix} 0 & 1 \\ -1 & 0 \end{pmatrix}, \begin{pmatrix} 0 & e^{i\bar{\phi}} \\ -e^{-i\bar{\phi}} & 0 \end{pmatrix} \right\}. \quad (\text{B29})$$

## 5. Ambient and Acoustic Noises

The acoustic noise can be divided into a stationary part and a nonstationary part, the former of which comes from a stationary source and can be treated analogously to the other noises that have been analyzed, while the latter is caused by random excitation that acts as a random kick in our noise power spectrum. The stationary part will include the scattering light noise from the acoustic vibration of the beam tube, as well as the phase shift caused by the seismic movement and the excited acoustic wave in the air, since our residual gas pressure is not low enough to stop the propagation. In contrast, the non-stationary state will include the acoustic wave excited by a temporary source, such as a small earthquake, a storm, or some internal excitation of the acoustic wave. LIGO adopts a non-analytic approach to estimate their contribution by injecting noise at the sensor locations and measuring the response in the signal to calculate the coupling function numerically for future predictions [105, 106]. And to the best of our knowledge, there is no analytical expression due to the complicated coupling mechanism. Therefore, we will adapt a compare-and-borrow approach to estimate the level of acoustic noise kick by identifying the configurations where VBG differs from LIGO semi-quantitatively. The environmental noises (e.g., wind coupling, magnetic influence, tube/chamber scattering, etc.) in VBG that are likely to have the same magnitudes due to a similar mechanism can be safely neglected, as they are expected to be well below the noise floor of VBG.

### a. Ground Excited Vibration of the Lenses/Mirrors

These noises usually occur in the low frequency region, while above 100Hz, the noises are dominated by the input beam jitter caused by the turbulence in the laser cooling system, which VBG will not have such a problem. All the measured and projected ambient noise of these is well below the sensitivity of LIGO [23, 105], and thus it will not be a problem for VBG if VBG has a similar coupling coefficient. For noise below 20Hz, the vibration noise can be effectively and actively sensed and canceled, the performance of which is mainly determined by the sensing noise. Natural seismic waves occur naturally at frequencies lower than this range [147]. Consequently, only nonstationary excitations between 20 Hz and 100 Hz, primarily from human activities, can surpass typical seismic and alignment noise, as shown in Fig. 9 (c). Mitigation involves deeply burying the lens/mirror nodes or choosing a quiet location. In addition, one can simply

avoid producing the signals within the noisy range by using chopping or adjusting the source frequency [123].

*b. Acoustic Wave in Residue Gas*

These effects are not considered in LIGO since it operates under an ultra-high vacuum, and these effects are completely negligible. A naive unit analysis based on coherent effects will tell us that this noise will scale as  $P$  instead of  $P^{1/2}$  in the thermal equilibrium case. A naive guess would be to simply scaling up the noise in LIGO by a factor  $10^7$ . However, this may not be accurate due to the cut-off pressure effect, which prevents the acoustic wave from propagating completely in the air. In this section, the order-of-magnitude estimation using the Jacobi-Anger expansion, following the treatment of diffraction by ultrasonic waves in the standard textbook [116], is performed to address this concern.

**Cut-off Gas Pressure.** When the residual gas pressure is low enough, the medium will no longer be viewed as a continuum and will thus stop the acoustic wave from propagating [148]. The attenuation factor of the sound wave in the residue gas can be approximated as [149]

$$\alpha \approx 1.4 \times 10^{-6} / \text{m} \left( \frac{f}{1\text{Hz}} \right)^2 \left( \frac{1\text{Pa}}{P} \right) \quad (\text{B30})$$

where the relaxation process due to  $O_2$  and  $N_2$  is not included (it will at most make the factor larger by 100 at low frequency, while the low gas pressure will suppress the cut-off frequency), which gives us a linewidth of

$$\Delta f \approx 5 \times 10^{-4} \text{Hz} \left( \frac{f}{1\text{Hz}} \right)^2 \left( \frac{1\text{Pa}}{P} \right). \quad (\text{B31})$$

This formula allows us to consider a new cut-off frequency where  $\Delta f < 0.1f$  corresponds to the requirement that the attenuation length be larger than the wavelength. Given that LIGO is operating at roughly  $10^{-7}$  Pa, the cut-off frequency of the sound wave can be as low as 0.01Hz, which has a wavelength of 30km and can never be excited within a tube section of 4km, assuming the sound wave in the residual gas will be stopped by the lens/mirror nodes. In the analysis below, we also set the minimum frequency of the sound wave, which is considered to be  $f_{\min} \approx 0.01$  Hz for extreme consideration, although most of the excitation should be well above this value. While considering the maximum frequency in VBG, one plugs in  $P = 1\text{Pa}$  to find that  $f_{\max} \approx 0.2\text{kHz}$ .

**Phase Shift.** At low pressure, the refractive index of the residual gas scales linearly with pressure  $P$  as [150]

$$n(P) = 1 + \alpha P, \quad (\text{B32})$$

where  $\alpha \approx 3 \times 10^{-9} / \text{Pa}$ . Let  $\gamma \equiv \frac{\delta \rho}{\rho}$  denote the fractional variation introduced by the acoustic wave, then the refractive index changes as

$$\delta n = \alpha \gamma P. \quad (\text{B33})$$

And thus, the effective optical path length gain of the fundamental mode is given by

$$\delta z_{\text{eff}} \approx L_{\text{eff}} \alpha \gamma P, \quad (\text{B34})$$

with  $L_{\text{eff}}$  denoting the effective length being influenced, which can be derived by assuming the coherent length for the sound wave is roughly its wavelength [151], followed by a Poisson process:

$$L_{\text{eff}} \sim \lambda_s \sqrt{\frac{L_0}{\lambda_s}} \approx \sqrt{\frac{L_0 c_s}{f}}. \quad (\text{B35})$$

Another way to see why this effective length shall be a good approximation is that it agrees with the square root of the autocorrelation function, assuming a plane wave over the whole length [152]

$$\frac{1}{\alpha P} \sqrt{\langle \delta n(x) \delta n(x') \rangle} \leq \sqrt{\frac{\lambda_s L_0}{2\pi}}. \quad (\text{B36})$$

Therefore, we are not left to determine  $\gamma$ . In fact, depending on how it is excited, it can be computed in two different ways:

1. If the acoustic wave is excited by some boundary oscillation (e.g., seismic movement) with  $z(f)$ , then by the continuum relation [148], one obtains

$$\gamma \approx k_s z(f) \approx 0.37 \times \left( \frac{f}{20\text{Hz}} \right) z(f). \quad (\text{B37})$$

2. If the acoustic wave is excited by some inner objects (e.g., some speakers) that produce  $L_{DB}$  noise under normal pressure conditions, then

$$\sqrt{\int \gamma^2(f) df} \approx \gamma(f) \sqrt{\Delta f} = \frac{\delta P}{P} = \frac{P_{\text{ref}}}{P} \times 10^{\frac{L'_{DB}}{20}}, \quad (\text{B38})$$

where  $P_{\text{ref}} = 20\mu\text{Pa}$  is the reference sound pressure in the air and

$$L'_{DB} = L_{DB} + 20 \log_{10} \sqrt{\frac{P}{10^5 \text{Pa}}}. \quad (\text{B39})$$

Combining everything together, one obtains

$$\gamma \approx 6 \times 10^{-8} \times 10^{\frac{L_{DB}}{20}} \sqrt{\frac{1}{\Delta f}} \sqrt{\frac{1\text{Pa}}{P}} \quad (\text{B40})$$

And thus, the effective optical path shift can be written as

1. Boundary excitation:  $2 \times 10^{-8} \sqrt{\frac{f}{1\text{Hz}}} \left( \frac{P}{1\text{Pa}} \right) z(f)$
2. Inner excitation:  $2 \times 10^{-13} \text{m} \times 10^{\frac{L_{DB}}{20}} \sqrt{\frac{1\text{Hz}}{f \Delta f}} \sqrt{\frac{P}{1\text{Pa}}}$ .

Notice that the first expression reproduces the  $P$  dependent, as indicated by our unit analysis, while for inner excitation, the dependent seems to still be  $\sqrt{P}$ , but, in fact, it is hidden in the dependent of  $\Delta f$ .

The boundary excitation may represent a stationary part of the acoustic sound noise and requires us to compare it with the seismic and alignment noise. The coupling factor given by the boundary excitation grows with  $\sqrt{f}$ , and for the maximum frequency  $f_{\max} = 200\text{Hz}$ , it is roughly  $3 \times 10^{-7}$ . When one compares it to the maximum suppression factor, given by the passive isolation, which is no more than  $10^{-4}$ , we expect that this effect is dominated by the performance of the passive isolation platform.

As for inner excitation, we will still need the linewidth of the sound wave excitation. Typically,  $\Delta f \approx \frac{c_s \alpha}{2\pi}$  with  $\alpha$  being the attenuation factor of the sound wave in the residual gas. Using Eq. (B30), we have

$$\delta z_{\text{eff}} = 2 \times 10^{-11} \text{m} \times 10^{\frac{L_{DB}}{20}} \left( \frac{1\text{Hz}}{f} \right)^{\frac{3}{2}} \left( \frac{P}{1\text{Pa}} \right) \quad (\text{B41})$$

Since above  $f = 1\text{Hz}$ , the alignment noise roughly grows with  $1/f$ , the significant point for reference will be  $f = 1\text{Hz}$ , which gives us

$$\delta z_{\text{eff}}(1\text{Hz}) \approx 2 \times 10^{-11} \text{m} \times 10^{\frac{L_{DB}}{20}}, \quad (\text{B42})$$

For a typical value, we consider the noise level to be  $L_{DB} = 20\text{dB}$ , which corresponds to a relatively quiet office. Compared to the value  $2 \times 10^{-9} \text{m}/\sqrt{\text{Hz}}$ , we see that the noise will be dominated by the seismic movement at low frequency, while it may contribute significantly when  $f > 10\text{Hz}$ , thus affecting the high frequency performance before its cutoff frequency at  $200\text{Hz}$ . In addition, this noise acts as a scatter in the PSD and can be safely avoided by making the signal off-resonant to the excited frequency. The noise level of the residue gas is plotted in Fig. 8 as scatter points for comparison.

**Mode Loss.** The acoustic wave may also introduce mode loss, which can be approximated using the Jacobi-Anger approximation as [116]

$$l_{ac} \sim 1 - J_0^2(m) = \frac{m^2}{2}, \quad (\text{B43})$$

where  $m = k\delta z_{\text{eff,rms}}$  is the modulation depth. For the boundary excitation, it is surely not a problem since the loss shall be dominated by the misalignment level determined by the performance of the two stage platform. While for inner excitation, one obtains for the extreme case  $f_{\min} = 0.01\text{Hz}$ ,

$$l \approx 4 \times 10^{-11} \times 10^{\frac{L_{DB}}{10}} \left( \frac{1550\text{nm}}{\lambda} \right)^2. \quad (\text{B44})$$

As the level of loss in each section is at least 10ppm, the effects will not need to be considered as long as  $L_{DB} \leq 60\text{dB}$ , which is already a very noisy environment.

## 6. Active Noise Cancellation

Applying phase noise sensing and active cancellation is a common practice to suppress noise at low frequencies. This kind of cancellation is conducted by the so-called Doppler cancellation techniques [153], which interfere with the round-trip beam and the local beam to estimate the phase noise.

Let  $\phi(t)$  denote the one-way phase noise at time  $t$  before cancellation. Assuming the channel is reciprocal, we have

$$\phi_{RT}(t) = \phi(t) + \phi(t - \tau), \text{ with } \tau = \frac{L}{v}, \quad (\text{B45})$$

where  $L$  is the one-way distance and  $v$  is the velocity of the light beam inside the channel. For VBG, it is roughly just the vacuum light velocity  $c$ . The correction is performed by dividing the estimation of  $\phi_{RT}(t)$  by two:

$$\hat{\phi}(t) = \frac{1}{2} \phi_{RT}(t) + \phi_n(t), \quad (\text{B46})$$

where  $\phi_n(t)$  denotes the noise for sensing the correction. And thus, the residual noise is given by

$$\phi_{\text{res}} = \phi(t) - \hat{\phi}(t), \quad (\text{B47})$$

The Fourier component, which is then given by

$$\tilde{\phi}_{\text{res}}(f) = \frac{1}{2} [1 - e^{-i2\pi f\tau}] \tilde{\phi}(f) + \tilde{\phi}_n(f). \quad (\text{B48})$$

Therefore, the PSD of the residual noise is related to the original PSD by [154]

$$S_{\phi,\text{res}}(f) = \sin^2(\pi f\tau) S_{\phi}(f) + S_{\phi,n}(f). \quad (\text{B49})$$

We see that when  $f \ll \frac{1}{\tau}$ , there is a suppression of the noise, and this formula agrees well with the one in reference [155, 156] within a constant factor  $\frac{4}{3}$ . However, when  $f > \frac{1}{\tau}$ , there will be hardly any suppression on average, which defines the cut-off frequency  $f_{\max} = \frac{1}{\tau}$  and agrees with our intuition.

The sensing noise depends on the sensing laser's power and linewidth via [157],

$$S_{\phi,n} = \left( \frac{hc}{\lambda\eta P_s} + S_\nu \frac{4\sin^2(2\pi f\tau)}{f^2} \right) \times \left( \frac{\lambda_s}{\lambda} \right), \quad (\text{B50})$$

Here, the first term in the parentheses represents shot noise, with  $P_s \approx 1\mu\text{W}$  being the receiving power and  $\eta \approx 0.8$  representing the detection efficiency. The second term represents laser frequency noise, which dominates the performance. We assume that an ultra-stable laser with  $S_\nu \approx (6.4 \times \frac{10^{-5}}{f} + 1.4 \times 10^{-4}) \text{Hz/Hz}$  [158] and a wavelength  $\lambda_s \approx 1542\text{nm}$  is being used for sensing by default. Alternatively, a cheap stabilized laser with a Hertz level linewidth achievable using an 80s technique will also work, but with less satisfactory performance and an rms phase noise to the level of  $1\text{mrad}$  [159, 160].

The delay  $\tau$  depends on the concrete correction scheme. One can sense phase noise all the way to the end of the propagation by reflecting the sensing beam back, which allows for lower sensing error and minimal modifications to the VBG system. However, this will seriously limit the suppression bandwidth: assuming  $L = 10^4\text{km}$ , the scheme will not work when  $f > f_{\max} \sim 10\text{Hz}$ . An additional scheme may involve sensing the phase noise in sections and combining the sensed noises to perform post-subtraction. In this case,  $L = L_0$  and  $f_{\max} \sim 100\text{kHz}$  and the overall PSD is just the section PSD scaled with  $\sqrt{L}$ . However, this will require one to extract and sense the sensing beam at the end-point nodes of each section, which will require routing techniques. In principle, this can be done by encoding the sensing beam into different frequency modes or polarizations [161, 162] and then using a special coating or a polarization-based beam splitter, which is probably being deployed at the reflector section. If the signal beam is a fragile quantum signal, stringent requirements will be imposed on these devices to maintain the performance of the VBG. But the good news is that the sensing beam itself will not demand a high-quality channel, as it can be classical and does not need to propagate over long distances.

Another way to avoid the influence on the signal beam is to separate the sensing beam path and the signal beam path, i.e., by using an additional channel that is rigidly bound to the signal channel to approximate the signal channel error. In this case, the influence can be minimized because there are almost no additional components to add to the signal beam path. However, the sensing error  $S_{\phi,n}(f)$  might be larger than the estimated floor induced by the sensing laser, as it will be challenging to sense the actual phase noise induced by residual gas or the thermal movement of the mirror experienced by the signal beam. In addition, as the path sensing beam roughly needs to be separated by a distance,  $d_{ss}$ , of at least a radius of the lens from the signal beam, the relative tilting angle between the signal beam and the sensing beam will couple into the parallel movement noise via the factor of  $d_{ss}$ . Luckily, this issue can be suppressed by various techniques, including separating the main sensing beam into different paths around the signal beam to reduce the effective  $d_{ss}$ , using an imaging system [163], or a retroreflector [120–122].

We assume that the separated and section-wise sensing is the default scheme for VBG calculation. The actual measured experimental performance may deviate from the theoretical limit given by Eq. (B50) due to other potential noise mechanisms. A good reference is the estimated noise level based on the actual measured data [164] from LIGO’s multi-color arm length stabilization system [38, 165, 166], which utilizes the Pound–Drever–Hall (PDH) method [159] to coarsely control the detuning induced by the cavity arm length fluctuation, bringing the system from free status into operation. The result is shown in the orange curve of Fig. (8), which lies between the performance limit induced by the ’17 advanced laser

and the 80s laser, being one order of magnitude larger than the previous. The noise is primarily dominated by acoustic noise and angular fluctuation noise, which are intrinsic to their scheme and can be suppressed with increasing effort. Therefore, we expect that the default estimated noise level is reasonable and achievable with current techniques.

### Appendix C: Performance of Memory Configuration

It is not surprising that VBG can be considered a very large high-Q optical cavity, as its initial motivation, LIGO, is such. The idea of employing an optical cavity as quantum memory has long been investigated [167, 168], the principle of which is to use the techniques from building a Q-Switch cavity [47, 169] to implement the read and write operations. Employing sections of VBG as quantum memory (VBGQM) will be particularly convenient and suitable for quantum communication protocols that require memory and are executed on VBG. VBGQM has advantages in that it has a very broad bandwidth, a sufficiently long storage time, can be operated at room temperature, and does not require conversion into matter qubits. Some particular designs for VBGGM are shown in Fig. 12. The performance of VBGQM can also be characterized by the attenuation and the dephasing of the optical quantum state after a storage time of  $T$ , where the decay of the probability of successful retrieval of the quantum state can be written as

$$P_{\text{success}} = \exp(-\alpha_{\text{tot}}cT), \quad (\text{C1})$$

with  $\alpha_{\text{tot}}$  being the attenuation factor. For the memory configuration, the beam is reflected using a configuration similar to S45M. Assuming a mechanical switch is used, then the angle alignment is essential and dominates the attenuation factor, as

$$\alpha_{\text{tot}} \approx -\frac{10}{L_0} \log_{10}(1 - 2k^2\omega_0^2\delta\beta^2) \sim 3.5 \times 10^{-4} \text{dB/km}, \quad (\text{C2})$$

for  $\delta\beta \sim 10^{-7}\text{rad}$  and  $L_0 = 4\text{km}$ . While for the EOM/PBS switch, the loss is dominated by these optical elements, which will introduce a loss at 0.1% level [170], and thus an effective attenuation factor of  $1 \times 10^{-3}\text{dB/km}$ . What’s worse is that in the VBGQM case, the static misalignment of the two mirrors will tend to yield coherent effects, as the pulse will be reflected back and forth within the same section, breaking the stochastic accumulation assumption. In this case, we shall consider the neighboring mode  $(0, \pm 1)$  and write the beam as a vector, including the information for both mode spaces as

$$\vec{E} = \begin{pmatrix} E_{00} \\ E_{0|\pm 1|} \end{pmatrix}, \quad (\text{C3})$$

after which, the truncated conversion matrix up to the second order of the mirror  $M_i$  misalignment angle  $\delta\beta$  can

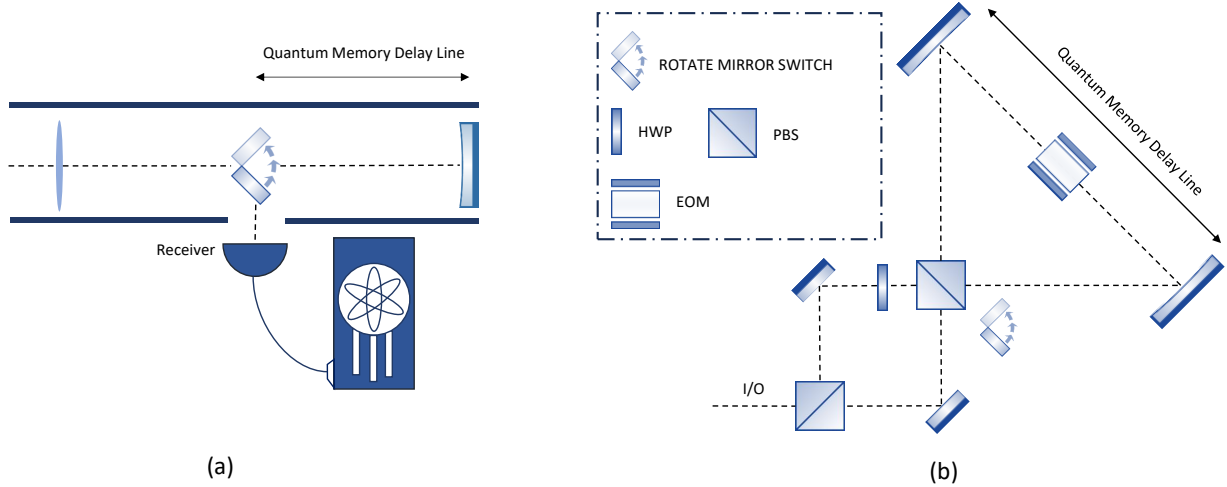


FIG. 12. The simple illustration for the designs of VBGQM. (a) A simple design utilizes a mechanical rotating mirror to perform the I/O operation to the VBGQM. The memory delay line is a section of VBG (b) A more complicated design with either an electro-optic modulator (EOM) or mechanical rotating mirror to perform the I/O operation, the former may enable ultrafast switch time but may also introduce an additional 1% loss per cycle which may seriously harm the performance of VBGQM. The memory delay line is also a section of VBG, but with lenses on both sides replaced by mirrors.

be derived as [117]

$$M_i = \begin{pmatrix} \sqrt{1 - \frac{1}{2}\gamma_i^2} & \frac{\sqrt{2}}{2}i\gamma_i \\ \frac{\sqrt{2}}{2}i\gamma_i & \sqrt{1 - 2\gamma_i^2} \end{pmatrix}, \quad \gamma_i \equiv k\sqrt{2}\delta\beta_i w_i, \quad (\text{C4})$$

with  $w_i$  being the spot size at the mirror's location. In addition, the propagation matrix between the two mirrors can be written as

$$L_p = \sqrt{1 - l_{\text{other}}} \begin{pmatrix} 1 & 0 \\ 0 & e^{i\phi_g} \end{pmatrix} \quad (\text{C5})$$

where  $\phi_g$  is the Gouyo phase [171, 172] determined by the separation between the two mirrors, and  $l_{\text{other}}$  is the other loss that is not related to angular misalignment. Therefore, the round-trip process can be described by the following product of the conversion matrix,

$$C_{\text{cavity}} = M_1 L_p M_2 L_p^\dagger. \quad (\text{C6})$$

If we assume the configuration shown in Fig. 12(a), where half of a standard VBG section is used for quantum memory with a plane mirror acting as the switch, then the attenuation performance of the VBGQM with static angle misalignment is shown in Fig. 13 in comparison to the stochastic assumption. We observe that the effective storage time is shortened by two orders of magnitude due to coherent interference for both the common and reversed tilting cases. One may wonder whether we can convert the power in  $(0, \pm 1)$  mode back to the  $(0, 0)$  mode to avoid this effect. Unfortunately, this will require precise knowledge of the misalignment angle and advanced

spatial mode conversion techniques, the latter of which may introduce additional losses.

In addition, we note that the cycle time of VBGQM is limited by the length of the VBG section and the speed of the I/O switch, i.e.  $\tau_c \geq \text{Max}(\tau_{\text{switch}}, 2\frac{L_0}{c})$ . In general, the round-trip time for a single VBG section will be approximately  $30\mu\text{s}$ , which dominates the switch time regardless of whether an EOM switch or a mechanical switch is used. The trade-off between cycle time and total storage time has long been considered a serious drawback of this kind of cavity-based optical storage. We can also estimate the number of modes for frequency division multiplexing inside a VBGQM using the free spectral range  $\delta\nu$  for a simple cavity as

$$\#\text{Modes}_{\text{FDM}} = \frac{\Delta\nu}{\delta\nu} = \frac{2L\Delta\lambda}{\lambda^2} = 3 \times 10^8, \quad (\text{C7})$$

which shows a tremendous capacity to store the optical quantum signal of different frequency modes simultaneously. Another way to understand Eq. (C7) is that we require the pulse length of the encoded bosonic information to be shorter than  $L$  to keep it completely stored inside the cavity. While the ability to perform time division multiplexing will be limited by the speed of the switch if each pulse needs to be controlled independently, the maximum number of pulses that can be stored inside the VBG cavity can be expressed as

$$\#\text{Modes}_{\text{TDM}} = \frac{2L_0}{c\tau_{\text{switch}}}. \quad (\text{C8})$$

For a mechanical switch that operates at the microsecond level, only tens of pulses can be stored. However, if all

pulses are stored for the same time, then the maximum number of pulses will again be limited by the duration of the pulse  $\tau_p$ . In contrast, for the EOM/PBS switch, the switching time can be comparable to, or even shorter than, the pulse duration [173].

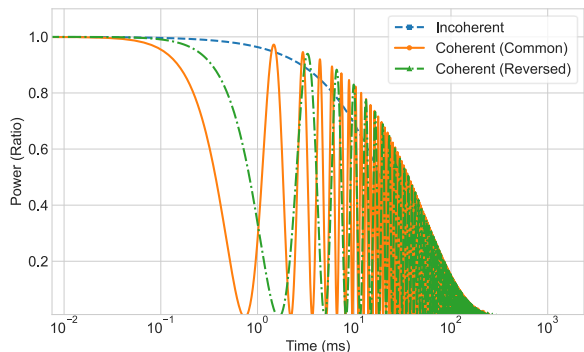


FIG. 13. The residue power ratio in the fundamental mode versus storage time of VBGQM assuming coherent effects of common static tilting and reversed static tilting with an angle  $\delta\beta$  for the two mirrors compared to the stochastic scheme.

As for the phase noise, the situation is a little trickier than in the transmission case, as the light is not bouncing back-and-forth within the same section with a round-trip time  $\tau = \frac{2L}{c}$ , and the noises may add up coherently instead of following a Poisson process. Here, we adapt a similar technique to relate the phase noise PSD of the signal after being stored for  $N$  cycles to the phase noise PSD caused by a single round trip  $S_{\phi_r} \approx 2S_{\phi_L}$ . The latter represents the single section phase noise PSD of the VBG channel, which can be calculated by multiplying Fig. 8 with  $L = 4\text{km}$ . Let  $\delta\phi_r(t)$  denote the simple round phase noise at time  $t$ , then the total phase noise is estimated as

$$\delta\phi(N) = \sum_{n=0}^{N-1} \phi_r(n\tau). \quad (\text{C9})$$

In the frequency domain, the time delay acts as a phase shift factor  $e^{-i2\pi fn\tau}$ , after which one performs the sum to obtain the transfer function

$$|H(f)|^2 = \frac{\sin^2(N\pi f\tau)}{\sin^2(\pi f\tau)}, \quad (\text{C10})$$

and the PSD of the signal is related to the PSD of the single round-trip phase noise PSD as

$$S_{\phi}(f) = 2S_{\phi_L}(f) \frac{\sin^2(N\pi f\tau)}{\sin^2(\pi f\tau)}. \quad (\text{C11})$$

This relation can also be derived by viewing the VBG cavity as an F-P etalon and calculating the final phase response. When  $f \ll \frac{1}{\tau}$ , the pulse experiences coherent

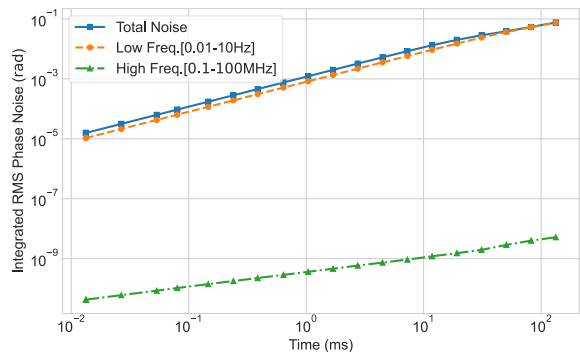


FIG. 14. RMS phase noise of VBG integrating over the whole phase noise PSD versus storage time after active cancellation and the contributions from low frequency and high frequency.

noise at each round. Thus, the effective transfer factor is  $N^2$ , representing a quadratic decay. In the high-frequency region,  $f \gg \tau$ , the average value of this factor matters since the function oscillates quickly. Therefore, we find that

$$|\overline{H^2}| \propto \frac{1}{2\pi} \int_{-\pi}^{\pi} \frac{\sin^2(Nx)}{\sin^2(x)} dx = N, \quad (\text{C12})$$

which represents linear growth corresponding to a Poisson process and can be understood as the high-frequency noise at different cycles not being correlated. Luckily, unlike the VBG channel case, the sensing of the error and, thus, the active noise cancellation are not limited by the round-trip delay since they are performed locally. In principle, the error can be sensed in real time and with  $\tau \sim 1\mu\text{s}$  in Eq. (B49), limited by the sensing time. The noise after cancellation is now just the residual gas noise and the mirror thermal noise. The RMS noise of the VBG memory channel versus storage time, integrating over the  $0.01 - 10^8\text{Hz}$  together with the contributions from low and high frequency, is shown in Fig. 14, the scaling of which matches our previous prediction.

#### Appendix D: Enhancement of Frequency Transfer

The investigation of frequency transfer has persisted over several decades [36] due to its profound significance in the field of metrology. This endeavor has seen continual advancements in accuracy, exemplified by the implementation of extensive fiber optic linkages [153, 155, 156, 174, 175] as well as, more recently, through atmospheric free-space connections [176]. A critical aspect of evaluation in such systems is the additional fractional frequency instability introduced by the transmission channel. This instability is traditionally quantified by measuring the interference of an ultra-stable laser's signal after it reflects back from completing a round-trip

journey. The results are typically presented quantitatively in terms of the modified Allan deviation (MDEV).

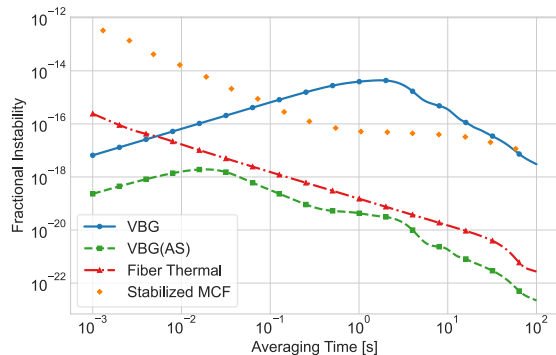


FIG. 15. Added fractional frequency instability over 25km transmission of VBG with and without active noise cancellation quantified by modified Allan deviation under different averaging time in comparison to the fiber thermal floor [41–43] and the state-of-the-art multi-core fiber (MCF) frequency transfer experiment data [177].

As one may expect, a larger phase noise in the link is coupled into a larger frequency noise in the Fourier domain via a  $f^2$  factor. Therefore, one can show that the MDEV can be calculated from the PNPSD in the continuous limit via [19, 178]

$$\sigma_y^2(\tau) = \frac{2}{\nu_0^2} \int_0^\infty S_\phi(f) \frac{\sin^6(\pi f \tau)}{(\pi \tau)^4 f^2} df, \quad (\text{D1})$$

with  $\tau$  as the averaging time and  $\nu_0$  as the carrier frequency. Figure 15 presents the VBG performance derived from the PNPSD, with and without active noise cancellation, alongside fiber transfer results[177]. The  $-1$  slope of both the fiber thermal floor and VBG with active noise cancellation indicates  $1/f$  Flicker noise, attributed to spontaneous length fluctuations and frequency noise, respectively, occurs at low frequencies [43], while the  $-3/2$  slope in both the stabilized MCF signifies white phase noise. The minor hump in both VBG curves arises from the rapid roll-off of the seismic noise. The figure illustrates that VBG delivers superior short-term stability with low high-frequency noise compared to fiber techniques, even in the absence of active noise cancellation, and achieves optimal stability, surpassing the fiber thermal floor by at least two orders of magnitude when active noise cancellation feedforward is employed.

### Appendix E: Performance Analysis of Additional Protocols

We summarize the key performance metrics of VBG and how the mentioned protocols depend on them in Table. II as a supplement to Fig. 3 in the main text.

## 1. Quantum Position Verification

Position verification is also an interesting task of significant practical importance. In many real-world scenarios, the server may want to confirm that the clients are located within the area that complies with the service contract, while the clients may not always be honest. The position verification can be performed by exploiting the limitations imposed by special relativity, similar to Relativistic-QKD [58]. For simplicity, we consider only the one-dimensional case and suppose the two verifiers, separated by  $L$ , want to verify that the client is indeed located in the middle between them. A typical method to do that is shown by Fig. 16, where the prover is asked to compute a function that requires both inputs to be transmitted at the speed of light from the two verifiers and to return it in time so that the overlap of the light cones confines its location. However, since classical information can be copied, the two attackers can easily emulate a fake position by exchanging their received inputs. It has been proven that there is no secure classical position verification [179].

The situation can be avoided by exploring a similar idea from quantum key distribution, where the quantum nature automatically prohibits perfect copying. And numerous research studies have been conducted [60–62]. And we consider a hallmark protocol that is executed as follows [61]:

1. **Random Generation.** The Verifiers  $V_0$  and  $V_1$  choose two strings of random bits  $v_0, v_1$  of length  $n$  and let  $f$  be the inner product function.
2. **Quantum State Transmission.** If  $f(v_0, v_1) = 0$ ,  $V_0$  prepares a qubit  $Q$  in the  $Z$  basis. Otherwise, prepare it in the  $X$  basis.
3. **Classical Bit Transmission.**  $V_0$  and  $V_1$  send  $v_0$  and  $v_1$  to the Prover  $P$  and engineer the timing so that  $Q, v_0, v_1$  reaches the position  $z$  they want to verify at the same time.
4. **Measurement.** If  $f(v_0, v_1) = 0$ , the prover measures  $Q$  in the  $Z$  basis. Otherwise, measure it in  $X$  basis.
5. **Certification.** The Prover sends back the measurement results  $b$  to the two verifiers immediately after receiving  $Q$  at the speed of light.
6. **Verification.** The verifiers check whether the measurement result is correct and whether the measurement result arrived in time. Then, repeat the above procedure for  $r$  rounds to achieve the desired confidence.

In contrast to the QKD case, verifiers in QPV cannot trust anyone; therefore, attackers may also use entanglement to attempt to hack the protocol. It has been

TABLE II. Summary of VBG's Performance Metrics and Applications Requirements\*

Metrics	Attenuation (dB/km)	Linewidth (THz)	Phase (rad/ $\sqrt{\text{km}}$ )	Polar. (Prob/km)	Trans. Speed (c)	Pulse Dur. (fs)
VBG Data	$\sim 4 \times 10^{-5}$	$\sim 6$	$\sim 2 \times 10^{-5}$	$\sim 1\text{ppm}$	$\sim 1 - 10^{-5}$	$\geq 50$
<b>Secure Quantum Communication</b>						
DI-QKD [49–57] (Sec. III A)	✓	✓	–	○	–	–
QPV [60–62] (Appendix E 1)	✓	✓	–	○	✓	–
R-QKD [31, 58] (Appendix E 2)	✓	✓	✓	–	✓	–
QPQ [59] (Appendix E 2)	✓	✓	–	–	–	–
MPED [63–67] (Appendix. E 2)	✓	✓	–	–	–	–
<b>Distributed Quantum Sensing</b>						
QTelescope [68–70] (Sec. III B)	✓	○	✓	–	–	–
QCN [71–73] (Appendix E 3)	✓	✓	✓	–	–	✓
GOG [74–76] (Appendix E 4)	✓	✓	✓	–	–	✓
<b>Federated Quantum Computation</b>						
QDC [77, 78] (Appendix E 5)	✓	✓	–	–	✓	–
BQC [79, 80] (Sec. III C)	✓	✓	–	–	○	–
NLQC [81–83] (Appendix E 6)	✓	✓	–	–	–	–

\* '✓' means the specific application relies on a certain performance metric, while '–' infers that it is less relevant, and '○' suggests that it may depend on a concrete protocol.

shown that this is always possible if an exponential number of entangled qubits is shared between the two attackers [180]. However, the above protocol is proven to be secure if attackers control fewer than  $o(n)$  qubits under a reasonable computation time limitation [181].

The implementation of large-scale QPV protocols is mainly limited by the attenuation in transmitting the single qubit in each round, which introduces a non-zero failure probability estimated as  $0.5\bar{\alpha}$  for the honest prover, with  $\bar{\alpha}$  being the average attenuation. In addition, the attackers will still have a non-zero probability of success,  $1 - p_a$ , even under the assumption of limited quantum resources, and thus set a threshold for the attenuation. Suppose we require the honest prover to succeed and the attackers to fail with the same confidence level (CL), the expected rounds  $r$  can be calculated using Hoeffding's inequality as

$$r \geq -\frac{2 \ln(1 - \text{CL})}{(p_a - 0.5(1 - \eta))^2}, \quad 1 - \eta \geq 2p_a, \quad (\text{E1})$$

dividing which by the multiplexing factor  $\Delta\nu$  gives us the minimum execution time  $\tau_{\text{ex}} \approx \frac{r}{\Delta\nu}$  in units of seconds. For the inner product function, we selected  $p_a \approx 0.1$ , and we remark that although more advanced protocols have been developed to avoid this threshold, they come at a cost by demanding additional quantum operations, such as quantum non-demolition detection [62].

The minimum executive time,  $\tau_{\text{ex}}$ , versus the distance

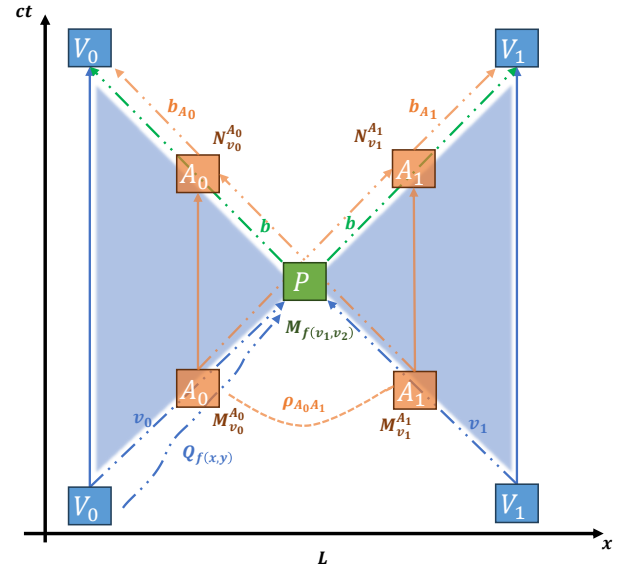


FIG. 16. Illustration for the typical QPV protocol. The shaded area represents the covering area of the light cones from both verifiers, with  $P$  being the only intersection point in the ideal case. And the orange boxes show the two possible attackers trying to fake the location using the pre-shared resource state with one-round simultaneous communication.

between the verifier and the honest prover, assuming the use of VBG for transmission, is shown in Fig. 17. It can be concluded that when the transmission distance is relatively short, the minimum execution time is at the picosecond level, which is mainly constrained by  $p_a$  determined by the protocol and also by the actual available multiplexing factor in practice. In this region, the execution time will be dominated by the transmission time, as the total time consumption for the protocol is given by

$$T_{\text{tot}} = \tau_{\text{ex}} + \frac{L}{\bar{v}_g}, \quad (\text{E2})$$

where  $\bar{v}_g \approx c$  is the transmission speed of the qubit through the vacuum beam guide. In addition, one sees that the threshold transmission distance is over  $10^4$ km if the QPV is executed via VBG, which shows that the VBG channel minimizes the influence of quantum transmission, as the execution of the protocol over such a continental scale will be limited by the Earth's curvature and the effective transmission speed of the classical bit strings.

Conversely, VBG could potentially facilitate the hacking of the QPV protocol because the known lower bound of qubits needed for attackers increases linearly with the classical bit strings sent, despite existing attack methods requiring a vast, exponential qubit count. Moreover, without quantum memory, attackers must transmit qubits nearly at light speed, which VBG can achieve, as demonstrated in Eq. (9) in the main text.

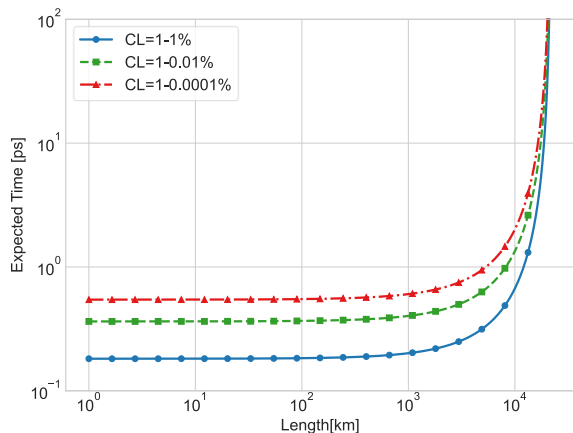


FIG. 17. Minimum execution time versus the distance between the verifiers and the honest prover under different confidence requirements.

## 2. General Quantum Cryptography

The two previously discussed tasks exhibit a hard attenuation threshold when advanced quantum control techniques are unavailable, demonstrating the irreplaceability of VBG in implementing these protocols in the

near term. In addition to these tasks, VBG enables fast quantum information exchange on a global scale, providing universal benefits for general quantum cryptography involving geographically isolated parties. Although these loss-tolerant protocols may be executed without VBG over long distances, the latter may still provide a speedup of several orders of magnitude compared to other existing quantum channel techniques. We will discuss a few more qualitative examples here.

Relativistic-QKD (R-QKD) [31, 58] has emerged as a focus within the QKD field due to its ability to maintain a nonzero key rate under significant channel loss and ensure security with minimal device assumptions through special relativity constraints. The optimal performance requires qubit trajectories to align as closely as possible with a null geodesic; otherwise, a quantum memory is necessary, and the channel must exhibit strong phase reliability. The quantum signal in VBG travels nearly at the speed of light in vacuum, in contrast to approximately  $\frac{2}{3}c$  in optical fiber. Furthermore, VBG can traverse a geodesic over  $10^3$ km with an effective refractive index  $n_{\text{eff}} \approx 1.001$  using the TMRRR configuration, in contrast to about 1.4 in satellite-to-ground links due to geographic constraints. This capability significantly benefits R-QKD implementation using VBG. Additionally, the VBG phase noise after active noise cancellation is below  $10^{-4}$ rad/ $\sqrt{\text{km}}$ , and VBG-based quantum memory (VBGQM) offers millisecond-level storage without qubit conversion, as detailed in Sec. IIC of the main text and Sec. C, addressing effective refractive index deviations and enhancing flexibility.

Following the spirit of QKD, the quantum private query (QPQ) protocol can be constructed with lure requests on a quantum server with quantum random access memory[59]. The randomly inserted lure request address, encoded in another base, allows the user to detect eavesdropping by the server with a high probability. VBG can be employed to transmit the request and the requested data with high fidelity, thereby reducing the possibility of the server faking its malicious behavior as channel loss.

Finally, multiparty entangled state distribution (MESD) across the large-scale network is also being actively explored due to its potential advantages in cryptography over pairwise established Bell pairs [182]. In particular, the quantum secret-sharing protocols[183, 184] can be uniformly described by the construction and manipulation of graph states over the network, which is a representative class of multiparty entangled states[185, 186]. Advanced and efficient network layer protocols [63–67] have been proposed for the general distribution of arbitrary graph states, where channel capacity and reliability play crucial roles in resource allocation and optimization. If the future network is built on the backbone of the VBG channel, then the network topology is approximately star-shaped, where any graph state can be distributed within one time slot, significantly mitigating the time delay for distribution and the pressure on quantum memory.

### 3. Synchronized Network of Clocks

As depicted in Fig. 18, constructing a highly precise synchronized quantum clock network (QCN) involves two key phases: first, aligning local clocks to a common ultra-stable frequency standard [72]; second, achieving precise clock positioning and synchronization through the Einstein synchronization method [187]. Research shows that quantum protocols can enhance both aforementioned processes, delivering a precision improvement by a square root scaling over classical techniques [71, 73]. In this framework, the deployment of VBG can provide substantial benefits in protecting the fragile quantum signal and serves as the foundation for constructing a quantum probe of gravity [188].

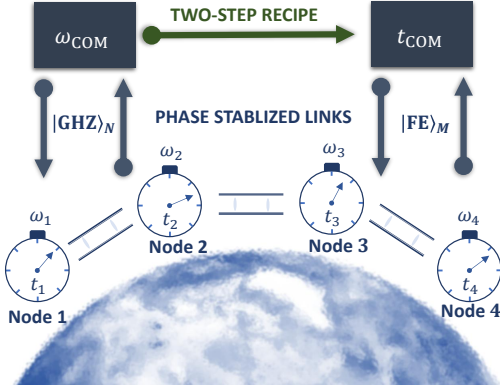


FIG. 18. Illustration of the quantum enhanced network of synchronized clocks which involves two key steps that benefits from different types of entangled state.

Establishing a remote frequency standard is critical for real-time sensing and many other experiments involving general relativity effects [189, 190]. Quantum entanglement can be utilized to construct a global frequency standard that leverages resources from all participating nodes, with optimal scaling for short-time Allan deviation as [72]

$$\sigma_y(\tau) \sim \frac{\sqrt{\log(N)}}{\omega_0 N} \frac{1}{\tau}, \quad (\text{E3})$$

where  $N$  is the total number of qubits involved in the GHZ state,  $|\text{GHZ}\rangle_N$ , and  $\omega_0$  is the frequency reference of the atomic clock. An intuitive way to understand it is that these established entanglements effectively bring the distributed local resources of each node together at the logical level and allow for the collective operations required for coherent quantum enhancement. This protocol requires a multiqubit GHZ state of extremely high fidelity ( $\sim 0.99$ ) and thus highly transparent channels, such as VBG, as any loss of photons destroys the GHZ state. In addition, establishing such a quantum clock network also requires robust frequency transfer between nodes to synthesize the global standard oscillator signal and implement feedback control. This is a purely classical and well-studied task [36], though VBG may also

provide potential enhancement due to its lower intrinsic phase noise compared to fiber when above 1Hz, which is discussed in more detail in Appendix. D.

Once the frequency of each node is locked to a common standard, the nodes can perform Einstein's protocol to eliminate the offsets of each clock. For simplicity, we assume a simple case involving two nodes, Alice and Bob, separated by a distance  $L$  while remaining in the same global inertial frame. The synchronization procedure works as follows:

1. Alice sends a pulse to Bob at  $t_a^s$ , as recorded by Alice's clock.
2. Upon receiving that pulse, Bob records the time  $t_b$  and reflects the pulse (or sends another pulse immediately).
3. Alice receives the reflective pulse and records the time as  $t_a^e$ .
4. The measured offset is determined as

$$\Delta t_{ab} = \left| \frac{1}{2}(t_a^s - t_a^e) - t_b \right|.$$

And the above procedure is repeated and executed in  $M$  parallel modes to achieve the desired precision.

The synchronization precision is reliant on the measurement accuracy of  $t_b$  and  $t_a^e$ . To streamline performance evaluation, we focus solely on the one-way transfer from Alice to Bob, assessing the variance of  $t_b$  as a positioning method, with an analogous analysis applicable for synchronization.

Using entanglement across  $M$  parallel modes can enhance measurement precision by  $\sqrt{M}$ . the frequency entangled (FE) state is assumed to be in the following form [71, 73].

$$|\text{FE}\rangle_M = \int d\omega \phi(\omega) \otimes_{i=1}^M |1_\omega\rangle_i, \quad (\text{E4})$$

where  $|1_\omega\rangle_i$  is the single photon state at frequency  $\Omega_i + \omega$  and  $\phi(\omega)$  is the spectral function shared by  $M$  modes, with  $\omega$  defined as the detuning with respect to the carrier frequency  $\Omega_i$ . Then, the variance of the measurement is given by

$$\Delta t_{\text{en}}^2 = \frac{\Delta \tau^2}{M^2}, \quad (\text{E5})$$

where  $\tau^2$  is the variance determined by the envelope function,

$$g(t) = \frac{1}{\sqrt{2\pi}} \int d\omega \phi(\omega) e^{-i\omega t}. \quad (\text{E6})$$

However, attenuation in the transmission channel can seriously impact the performance of the entangled state. Suppose that any one of the photons from the  $M$  modes

is lost. In that case, the state will be projected onto a diagonal density matrix in the  $|\omega\rangle$  basis, which is essentially a continuous wave instead of a pulse, and thus destroys any information regarding the arrival time [73]. Therefore, when the protocol is repeated for rounds  $r \gg 1$ , the asymptotic variance for the arrival time of each round can be calculated as

$$\Delta t_{\text{en}}^2 \simeq \frac{\tau^2}{\eta^M M^2}, \quad (\text{E7})$$

where  $\eta$  represents the coupling efficiency, as before. While in the classical case, the information of the mode whose photon is not lost is unaffected. Thus, we will have

$$\Delta t_{\text{cl}}^2 \simeq \frac{\tau^2}{\eta M}. \quad (\text{E8})$$

The different scaling dependence of  $\eta$  will give rise to the threshold value of coupling efficiency, below which the classical scheme is more advantageous. In addition, the channel will impose a phase noise  $\sigma_\phi^2$  as before. Besides, the broadening of the envelope due to GVD is estimated in Sec. IID of the main text. These two effects can be shown to be the same for both classical and entangled cases by transforming the field operators in the Heisenberg picture: The phase noise adds a time variance of  $\frac{\lambda^2 \sigma_\phi^2}{4\pi^2 v_g^2}$ , and the GVD broadens the variance of the envelope according to Eq. (11) in the main text.

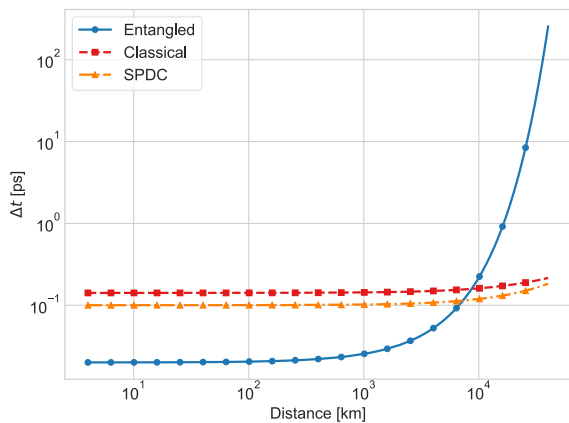


FIG. 19. Variance of the arriving time versus various separation length under classical,  $M$ -entangled state, and SPDC( $M = 2$ ) schemes. For the SPDC state, it is a partially entangled state separated into  $M/2$  tensor components, with each component containing two entangled photons.

For performance estimation, we set  $\tau = 1\text{ps}$  with  $g(t)$  as a Gaussian profile envelope function. Phase noise can be calculated using the PNPSD as before, and the mode numbers are determined by the linewidth of the VBG, assuming frequency multiplexing as  $M \approx \frac{\Delta\nu}{4\pi\tau} \approx 50$ . The synchronization precision using VBG at different separation distances  $L$  is shown in Fig. 19. The quantum

scheme grants roughly an order of magnitude enhancement over the classical scheme over a distance range of  $10^3$  km, whereas the performance significantly deteriorates over  $10^4$  km due to coherent loss. In addition, the SPDC scheme with two-by-two entanglement demonstrates a longer threshold distance, but with only an enhancement factor of  $\sqrt{2}$ .

#### 4. Giant Optical Gyroscope

VBG itself is a large-scale optical platform, and thus it is not surprising that it can provide advantages for measurements that benefit from scaling up, such as building a giant optical gyroscope (GOG). A quantum optical gyroscope has recently been proposed for seismology and to explore the interplay between quantum physics and general relativity [74]. An indistinguishable photon pair is emitted into a large ring cavity attached to the Earth's surface, with one photon propagating clockwise and the other counterclockwise. The rotation of the Earth, the speed of which is denoted as  $\omega_E$ , generates the Sagnac effect [191] and introduces a time delay  $\delta\tau_{\text{sag}}$  in the arrival time of two photons that is proportional to the area size of the ring cavity, which can be written as

$$\tau = \mathcal{F}A, \quad (\text{E9})$$

with  $\mathcal{F}$  being the sensitive factor and  $A$  being the area size. The delay  $\tau$  shifts the HOM dip from which the delay can be determined. In addition, general relativity predicts a correction in the locally observed angular rotation speed known as the frame-dragging effect [192],

$$\Delta\omega_{\text{FD}} = \frac{2GI}{c^3 R_E^3} \omega_E \sim 10^{-9} \omega_E \quad (\text{E10})$$

where  $G$  is the gravitational constant,  $I$  is the moment of inertia, and  $R_E$  is the radius of the Earth. This gives rise to a sensitive factor of  $\mathcal{F}_{\text{FD}} \sim 10^{-24}\text{s/km}^2$  and indicates that an effective area of  $10^6\text{km}^2$  can only generate a time delay at the attosecond level, which is barely within the reach of the demonstrated sensitivity of the HOM-dip measurement [193].

Such a measurement will certainly require ultra-transparent channels to keep those photons alive during propagation, where VBG comes into play. However, such a measurement also requires a relative precision of the order of  $10^{-9}$ , since it can be shown that there is no way to separate the frame-dragging correction from the normal angular rotation speed as long as the gyroscope is located on the Earth's surface. Although the gyroscope itself benefits from common noise rejection, this still imposes a stringent requirement for scanning over a delay line to achieve micrometer-level accuracy over a thousand-kilometer scale cavity. Nevertheless, we also need to further suppress the spreading of the photon pulse duration due to the GVD of the lens to reduce the width of the HOM-dip.

An alternative solution to this may be the employment of the active gyroscope technique, namely the intracavity phase interferometer (IPI) [194, 195], which measures the resonant frequency shift rather than the time delay itself, although it becomes a classical measurement scheme. Despite significant efforts devoted to constructing the first ground-based gyroscope for measuring the frame-dragging effect, they are still away from the required precision by two to three orders of magnitude [75, 76]. In addition to continuous wave measurement, it may be possible to combine and utilize a correlated frequency comb to further scale the system and eliminate the dead band due to cross-scattering, as the gain medium does not need to fill the entire cavity [196]. The precision of the measurement can also be improved using squeezed light [197], further exploring the potential of VBG channels.

### 5. Long-distance distributed fault-tolerant quantum computing

VBG technologies facilitate the development of long-range, distributed, fault-resistant quantum computing through the quantum data center (QDC), which minimally includes a QRAM and a quantum network interface, as presented in Fig. 20. The extremely low attenuation rate is vital for preserving coherence and reducing information loss across lengthy quantum channels [77, 109, 198]. In such applications, VBG could deliver  $T$ -gates efficiently with high quality and perform remote quantum computing fault-tolerantly, or perform remote distillation of magic states through high-fidelity entangling gates over long distances. This capability is essential for scalable quantum architectures that depend on modular and distributed subsystems. Such setups have been shown to offer significant advantages in terms of scaling with the size of the data and the efficiency of outsourcing computational tasks, with the presence of fast quantum memory [77, 199]. For instance, high-fidelity quantum teleportation will not only lead to low failure rates and higher-quality Bell pairs due to reduced attenuation but also enhance the robustness of quantum information transfer across distant nodes. This, in turn, will affect the *delay time* introduced in the distributed quantum computing setup [77, 78], where the delay of quantum communication plays a key role in determining the performance and architecture of surface code magic state distillation schemes.

Reduced communication latency and higher gate fidelities made possible by VBG will lead to lower delay times and more cost-effective magic state distillation protocols. For example, imagine that we have the distance  $d$ . The decay of the photonic intensity ratio will be  $10^{-d\alpha_{\text{att}}/10}$ . Suppose we have the speed of light  $c$ . Without photonic loss, the delay time will be  $d/c$ . Due to photonic loss, the delay time will be amplified by  $\frac{d}{c} \times 10^{d\alpha_{\text{att}}/10}$ . Thus, the relative delay time comparing

VBG with optical fiber is approximately  $10^{-d\alpha_{\text{att, fiber}}/10}$  for  $\alpha_{\text{att, fiber}} \gg \alpha_{\text{att, VBG}}$ . The longer the distance, the greater the advantage we gain in terms of relative delay time. For example, for  $d \approx 500\text{km}$ , we have a 31% saving in delay time. Such savings, according to Figure 3 of [78], will switch the optimal magic state distillation protocol and save around 20% qubits. Consequently, these improvements will enhance the overall throughput and scalability of distributed quantum computing and significantly improve the efficiency and reliability of quantum task outsourcing.

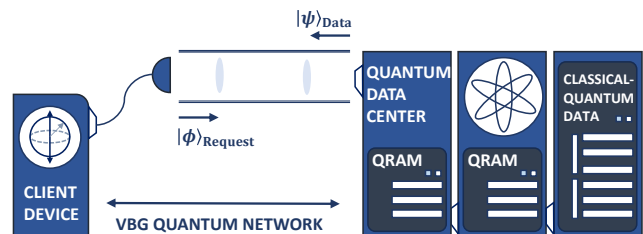


FIG. 20. Illustration of the interaction between quantum data center (QDC) and client’s processor via VBG-based quantum network.

### 6. Non-Local Computation Tasks

Robust entanglement establishment is also essential for performing non-local computation tasks, where quantum mechanics offers distinct advantages in reducing the cost of communication. In the QPV section, it was mentioned that hackers possess an exponential amount of quantum entanglement [180], which can, in fact, be modeled as a non-local computation task with one round of communication.

The general framework of non-local quantum computation (NLQC) was first proposed and pioneered by Yao *et al.* to investigate communication complexity in a quantum setting [81–83]: Let Alice and Bob receive local inputs  $x$  and  $y$  (either classical or quantum). Then, they are asked to compute a function  $f(x, y)$  distributively. That is, they are required to output  $a$  and  $b$  such that  $f(x, y) = a \oplus b$ . In the ideal case, if they possess a non-local box that is capable of computing  $f(x, y) = x \wedge y$  nearly perfectly (with a probability higher than 90.8%), it is shown that every function can be distributively computed with just one bit of information exchange [200, 201]. Notice that this is also exactly the case for the CHSH game, where a quantum strategy is capable of achieving an optimal success probability of approximately 85% [202]. Although this is not enough to trivialize the communication complexity, it still implies the advantages of nonlocal quantum computation.

In addition to hacking QPV, a representative application of non-local computation is coordinated decision-making through quantum telepathy, which can be ex-

exploited to establish an efficient stock market strategy beyond the classical limit [203]. However, if the entangled pair is being distributed via a direct photonic connection, the coupling efficiency  $\eta$  will seriously affect the performance of the protocol and establish a threshold below which the quantum strategy cannot develop any advantages. Simplifying the inputs for both parties to a single

bit, it can be shown that the threshold distance for fiber is limited to only 10 kilometers, where an instantaneous decision may not be necessary. However, if VBG is used for the distribution, the distance can be scaled to more than 30000 km, allowing HKEX and NYSE traders to carry out a quantum-enhanced coordinate trading strategy to maximize profits.